Formation, shape, and evolution of magnetic structures in CIRs at 1 AU

T. W. Broiles,[1,2] M. I. Desai,[1,2] and D. J. McComas[1,2]

Received 24 October 2011; revised 13 January 2012; accepted 22 January 2012; published 8 March 2012.

[1] We have surveyed the properties of 153 co-rotating interaction regions (CIRs) observed at 1 AU from January, 1995 through December, 2008. We identified that 74 of the 153 CIRs contain planar magnetic structures (PMSs). For planar and non-planar CIRs, we compared distributions of the bulk plasma and magnetic field parameters. Our identification of CIRs and their features yields the following results: (1) The different pressures within CIRs are strongly correlated. (2) There is no statistical difference between planar and non-planar CIRs in the distributions and correlations between bulk plasma and magnetic field parameters. (3) The mean observed CIR azimuthal tilt is within 1 σ of the predicted Parker spiral at 1 AU, while the mean meridional tilt is about 20°. (4) The meridional tilt of CIRs changes from one solar rotation to the next, with no relationship between successive reoccurrences. (5) The meridional tilt of CIRs in the ecliptic is not ordered by the magnetic field polarity of the parent coronal hole. (6) Although solar wind deflection is a function of CIR shape and speed, the relationship is not in agreement with that predicted by Lee (2000). We conclude the following: (1) PMSs in CIRs are not caused by a unique characteristic in the local plasma or magnetic field. (2) The lack of relationship between CIR tilt and its parent coronal hole suggests that coronal hole boundaries may be more complex than currently observed. (3) In general, further theoretical work is necessary to explain the observations of CIR tilt.

Citation: Broiles, T. W., M. I. Desai, and D. J. McComas (2012), Formation, shape, and evolution of magnetic structures in CIRs at 1 AU, *J. Geophys. Res.*, *117*, A03102, doi:10.1029/2011JA017288.

1. Introduction

[2] Co-rotating Interaction Regions (CIRs) were first observed by *Neugebauer and Snyder* [1966, 1967] as times of increasing solar wind speed and temperature, accompanied by enhancements in the plasma density and magnetic field strength that recurred with the solar rotation period. CIRs form when fast solar wind ($\sim$700 km s^{-1}) emanating from coronal holes at low heliographic latitudes pushes up against the slow solar wind ($\sim$350 km s^{-1}) ahead of it, creating a compression region in the heliosphere that co-rotates with the Sun [*Gosling and Pizzo*, 1999]. The CIR's compression region is three dimensional, often being approximated as locally planar with both azimuthal and meridional tilts [*Lee*, 2000]. Previous observational studies [*Clack et al.*, 2000; *Gosling et al.*, 1978, 1993; *Riley et al.*, 1996] of CIRs' three dimensional structure used data from Ulysses. This paper for the first time studies the local three dimensional tilt of CIRs at 1 AU over an entire solar cycle and compares observations to the predictions of *Lee* [2000] and *Pizzo* [1991] regarding CIR formation, shape, and evolution.

[3] In order to study the three dimensional structure of CIRs, we must also be able to relate the structure back to the observed bulk plasma and magnetic field properties within the CIR. *Jian et al.* [2006] performed a statistical survey of observed CIR properties from Jan. 1995 to Dec. 2004 using data from the Wind and ACE spacecraft. They identified a subset of 196 CIRs within a list of 365 stream interaction regions (SIRs), defined as interaction regions formed between fast and slow plasma streams that are not seen over multiple Carrington rotations. They identified CIRs by enhancements in total pressure, proton density and increasing solar wind speed across the event. *Jian et al.* examined the averages and standard deviations of the following CIR properties: (1) the peak total perpendicular pressure, (2) change in solar wind speed, (3) peak proton density, (4) peak magnetic field strength, and (5) the radial thickness. They also studied variations in these properties over the solar cycle, finding that compressions (magnetic field strength and total pressure) associated with CIRs were stronger during solar maximum.

[4] Figure 1 shows a sketch of the three dimensional surface between the fast and slow solar wind. This surface should depend upon the boundary between the coronal hole and the streamer belt in the solar corona [*Lee*, 2000]. The interplanetary magnetic field (IMF) aligns with the stream

[1]Department of Physics and Astronomy, University of Texas at San Antonio, San Antonio, Texas, USA.
[2]Space Science and Engineering Division, Southwest Research Institute, San Antonio, Texas, USA.

0148-0227/12/2011JA017288

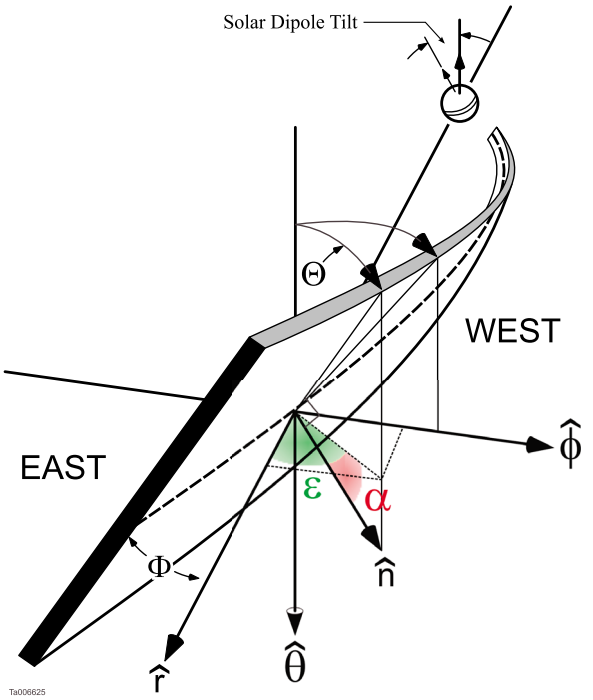

Figure 1. A sketch of a planar CIR, illustrating the relationship between CIR tilt and its coronal hole of origin. The angle, α, represents the meridional tilt out of the ecliptic and the angle ε, represents the azimuthal tilt in the ecliptic. Modified from *Pizzo* [1991].

interface of the CIR because it is a tangential discontinuity and by definition is impermeable by the magnetic field [*Belcher and Davis*, 1971]. The solar wind alters the magnetic field topology surrounding the stream interface in two ways; (1) deflected solar wind stretches the magnetic field components along the stream interface, and (2) the solar wind velocity component normal to the stream interface compresses the magnetic field in the same direction [*Intriligator et al.*, 2001].

[5] Realignment of the magnetic field along the stream interface can result in a planar magnetic structure (PMS). PMSs were first discovered in the solar wind by *Nakagawa et al.* [1989]. PMSs have been related to a number of different phenomena in the heliosphere such as the sheath ahead of fast interplanetary coronal mass ejections (ICMEs), magnetic sector boundaries, and CIRs [*Neugebauer et al.*, 1993]. *Clack et al.* [2000] studied the occurrence of PMSs within two CIRs at Ulysses, both of which were observed beyond 4 AU and at least 10° latitude above the ecliptic plane. They found qualitative agreement with *Gosling et al.* [1993] in that solar wind is deflected eastward and equatorward ahead of the CIR and westward and poleward behind the CIR. *Clack et al.* [2000] also observed that a CIR from the Northern coronal hole had a Southern tilt out of the ecliptic, while a CIR from the Southern coronal hole had a Northern tilt out of the ecliptic, as predicted for a simple dipole model of coronal hole structure [*Lee*, 2000; *Pizzo*, 1991].

[6] *Jones and Balogh* [2000] identified PMSs using the Ulysses data set between October 1990 and the December 1998, and found that the interplanetary magnetic field (IMF) is planar 9% of the time: either from heliospheric current sheet (HCS) crossings, ICMEs or interplanetary shocks. They found 58 planar CIRs, and concluded that CIRs between 1.5–5 AU commonly contained planar magnetic structures. They also found the average radial width of planar magnetic structures to be 0.13 AU.

[7] In this paper we examine CIR properties at 1 AU from the start of 1995 to the end of 2008. We identify 153 CIRs using a combination of an algorithm (see Appendix A) and rigorous visual inspection. Note that in the timeframe when our list overlapped with *Jian et al.* [2006] (1995–2004), all but one of our CIRs were also on their list. We find that almost half of the CIRs at 1 AU are sufficiently planar, enabling us to perform an analysis on their local planar structure. We also study the relationships between the bulk plasma and magnetic field properties within the identified CIRs. For CIRs with an identifiable planar magnetic structure, we study their tilt, scale size, and evolution over the solar cycle and the relationship to solar wind deflection. Finally, we examine how the observed local tilt compares with the theoretical predictions of *Lee* [2000] and *Pizzo* [1991], as well as with observational results from previous studies [*Clack et al.*, 2000; *Gosling and Pizzo*, 1999; *Jones and Balogh*, 2000].

2. Instrumentation, Event Selection, and Data Analysis

2.1. Instrumentation and Data Sets

[8] We use data from the Solar Wind Electron Proton and Alpha Monitor (SWEPAM) [*McComas et al.*, 1998] on the Advanced Composition Explorer (ACE) [*Stone et al.*, 1998], which provides ion distribution functions at a cadence of 64 s, and the Solar Wind Experiment (SWE) [*Ogilvie et al.*, 1995] on Wind [*Acuña et al.*, 1995] which provides the ion distribution function every 92 s. Ion distribution functions are used to calculate solar wind properties such as speed, v_p, density, n_p, and temperature, T_p. We also use data from the magnetometer (MAG) [*Smith et al.*, 1998] on board ACE, and the Magnetic Field Investigation (MFI) [*Lepping et al.*, 1995] on Wind. Both instruments provide the magnetic field vector, **B** every second. We use SWEPAM and MAG data when available, and use SWE and MFI data to study CIRs before the launch of ACE (Jan. 1, 1995–Jan. 23, 1998) and to fill gaps in the ACE data. We fill ACE data gaps using time-shifted SWE data from Wind. We used the X-only method defined by *Ridley* [2000], where the amount of time shift applied to data is estimated by the difference in radial distance from the Sun of the two spacecraft divided by the solar wind speed.

2.2. Event Selection

[9] In this study we compare observations of CIR three-dimensional structure with theoretical predictions using CIRs selected by an automated algorithm that also identifies the stream interface, and forward and reverse boundaries from Jan. 1995 through Dec. 2008, as described in Appendix A. We then visually inspect each event to ensure that the boundaries are appropriately selected and to identify the end of the high speed stream. Models of CIR formation [*Gosling and Pizzo*, 1999; *Lee*, 2000; *Pizzo*, 1991] do not account for

Table 1. A Description of Different Signatures Used to Identify CIRs Contrasted Against Those of ICMEs

Measurement	CIRs	ICMEs
Proton speed; v_p	Increasing across the interaction region [*Neugebauer and Snyder*, 1966].	Highly variable, steady decrease common from expansion [*Klein and Burlaga*, 1982].
Proton density; n_p	Elevated across interaction region, peak at or ahead of SI. Rarefaction occurring afterwards [*Neugebauer and Snyder*, 1966].	≤1 proton cm−3 in the ejecta. Shock and compression region in sheath surrounding fast ejecta.
Proton temperature; T_p	Tp increasing across the interaction region and remains high in fast solar wind [*Neugebauer and Snyder*, 1966].	Tp < 0.5*Texp in the ejecta. [*Gosling et al.*, 1973; *Richardson and Cane*, 1995].
He/p ratio	An increase from 4% to 5% at the SI. Decrease in variance after SI [*Borrini et al.*, 1981; *Wimmer-Schweingruber et al.*, 1997].	An increase in the ratio above 8% in the ejecta [*Hirshberg et al.*, 1972].
Magnetic field magnitude; |B|	Compression inside interaction region with peak at the SI [*Neugebauer and Snyder*, 1967].	>10 nT in the ejecta. A compression may occur in fast ICME sheath [*Klein and Burlaga*, 1982].
Magnetic field angles; θ, φ	A 180° change of azimuthal field often seen in or near a CIR [*Borrini et al.*, 1981].	Smooth rotation of magnetic field often present in magnetic clouds [*Klein and Burlaga*, 1982].
Total pressure; P_t	Increased pressure across the event with the peak possibly at the SI [*Jian et al.*, 2005].	Increased pressure may be present in ejecta and in the sheath [*Russell et al.*, 2005].
Plasma β	Little change, magnetic pressure and plasma pressure affected similarly.	β < 0.1 in magnetic clouds [*Klein and Burlaga*, 1982].
Suprathermal electrons	Narrow (<20°) anti-Sunward streaming in high speed stream. Counter streaming in some CIRs, beam widths typically differ by more than 40° [*Skoug et al.*, 2010].	Narrow (<20°) beams of bi-directional streaming along field lines [*Gosling et al.*, 1987].

CIRs with properties and structure that may have been influenced by nearby ICMEs [*Rouillard et al.*, 2009]. Although the exclusion of such events (∼41) may introduce a bias in our results, we believe that including CIRs with local plasma and magnetic field parameters that could have been distorted by such nearby ICMEs, would not constitute a true comparison with theoretical predictions. Therefore, we only use isolated CIRs that do not have ICMEs within at least 12 hours of their boundaries. We identify ICMEs using well known in-situ signatures [*Zurbuchen and Richardson*, 2006], the updated list of *Cane and Richardson* [2003] and the ACE and Wind shock lists (http://www.ssg.sr.unh.edu/mag/ace/ACElists/obs_list.html and http://www-istp.gsfc.nasa.gov/wind/current_listIPS.htm).

[10] Table 1 contrasts the in-situ properties of CIRs and ICMEs at 1 AU. These are: solar wind speed, proton density, proton temperature, the He/p ratio, magnetic field strength, magnetic field direction, total pressure and the ratio of thermal to magnetic pressure (i.e., the plasma β). The main differences between CIRs and ICMEs are: (1) the proton temperature is anomalously low in ICMEs, (2) the He/p ratio increases above 8% in ICMEs, (3) the plasma β decreases below 0.1 in magnetic clouds, a type of ICME [*Klein and Burlaga*, 1982], and (4) the suprathermal electrons stream bi-directionally along field lines in narrow (<20°) beams [*Gosling et al.*, 1987].

[11] Figure 2 shows a CIR that we identified using an algorithm that utilizes the signatures described in Table 1. From top to bottom, Figure 2 shows: solar wind speed (km s^{-1}) (Figure 2a), proton density (cm^{-3}) (Figure 2b), proton temperature (K), with expected temperature (K) in red [*Neugebauer et al.*, 2003] (Figure 2c), total pressure (pPa) [*Gosling et al.*, 1987; *Jian et al.*, 2006] (Figure 2d), magnetic field strength (nT) (Figure 2e), and solar wind deflection angles (°) (Figure 2g). In this example, the forward boundary is a shock, as indicated in Figure 2 by the vertical black line labeled FB, while the reverse boundary has not steepened into a shock (vertical blue line: RB). The stream interface and the end of the high speed stream are shown by vertical red lines labeled SI and HSS respectively. The four, distinct regions of the CIR are labeled: (1) uncompressed slow wind, (2) compressed slow wind, (3) compressed fast wind, and (4) uncompressed fast wind.

[12] We remark that the selection of CIR boundaries is somewhat subjective at 1 AU. Other studies have identified the stream interface as the location of a jump in entropy [*Borovsky and Denton*, 2010], a drop in O^{7+}/O^{6+} charge state ratio [*Wimmer-Schweingruber et al.*, 1997], or as the peak in total perpendicular pressure [*Jian et al.*, 2006], however these signatures frequently occur at different times within the CIR. For the example shown in Figure 2, multiple discontinuities might be considered as the location of the stream interface. For instance, the larger discontinuous drop in density at 1100 UT 07/05/07 is also a reasonable candidate for the stream interface. However, in our criteria we require that the stream interface be close to the shear in the azimuthal flow angle. This is because our study is focused on establishing the relationship between the PMS and the solar wind deflection and comparing with theoretical predictions. We remark that using a different time for the location of the SI would only affect the results shown in Figures 11 and 12 of this paper. Several studies [e.g., *Gosling et al.*, 1978; *Gosling and Pizzo*, 1999; *Lee*, 2000, and references therein] show that the stream interface is a tangential discontinuity in momentum balance, and can be identified by a shear in the solar wind flow angles. In other words, the stream interface deflects the fast solar wind in the opposite direction than it deflects the slow solar wind. We account for such deflections in our selection criteria by requiring that the azimuthal flow angle changes from positive to negative around the location of the stream interface. Note that at the time of the larger drop in density, the azimuthal flow angle is near maximum (∼5°) and was therefore not identified as a possible SI for this CIR.

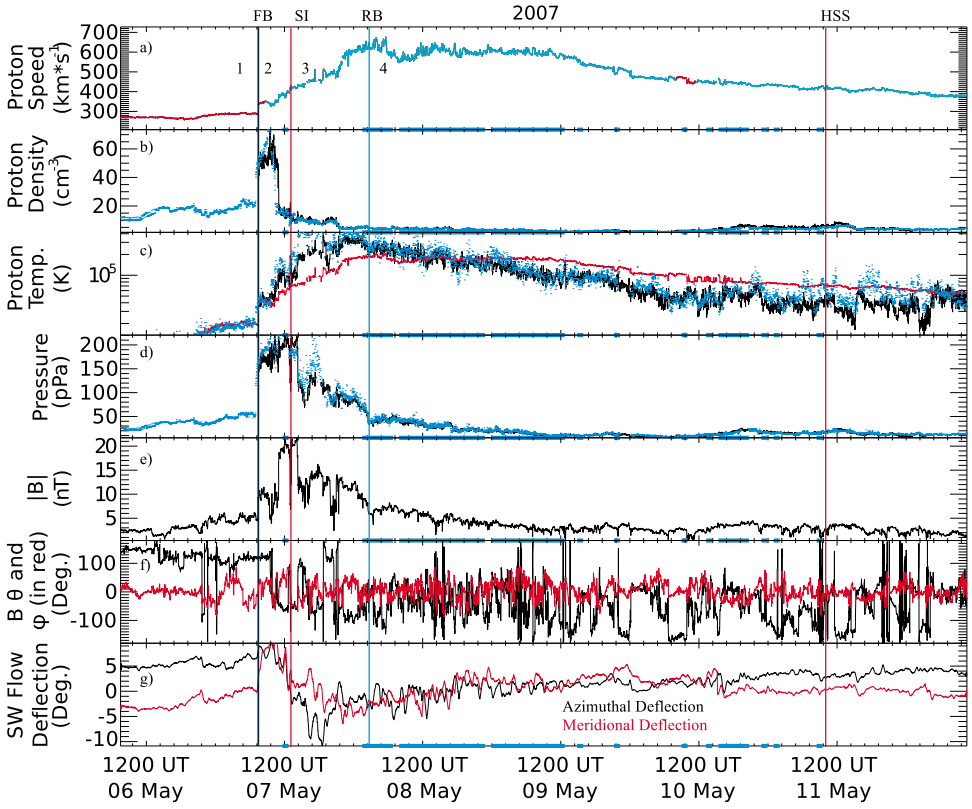

Figure 2. An example of a CIR from May 7, 2007 (CIR # 121 in Table 2). (a) Solar wind speed (km s^{-1}), (b) density (cm^{-3}), (c) temperature (black) and expected temperature (red) (K), (d) total pressure (pPa), (e) magnetic field strength (nT), (f) magnetic longitude (black) and latitude (red) (°), and (g) azimuthal (black) and meridional (red) solar wind deflection angles (°). The numbers 1–4 in Figure 2a identify the four regions of the CIR: (1) slow uncompressed, (2) slow compressed, (3) fast compressed, and (4) fast uncompressed. Vertical black line: forward boundary (FB), vertical red line: stream interface (SI), vertical blue line: reverse boundary (RB), and second vertical red line: the end of the rarefaction region (HSS). Solar wind speed data are colored red or blue to represent outward or inward IMF polarity respectively. Time shifted Wind data (blue) is shown for proton density, temperature, and total pressure. Thick blue ticks at the bottom of each panel represent times when Alfvénic fluctuations are present (see text for more details).

[13] The thick blue bar at the bottom of each panel of Figure 2 indicates times of observed Alfvénic fluctuations, which is a known property of the fast solar wind [*Belcher and Davis*, 1971]. We identify Alfvén waves by searching for intervals with strong correlation between the magnetic field and solar wind velocity fluctuations [*Belcher and Davis*, 1971]. We use intervals of 60 data points and require the absolute value in the average correlation coefficient between all three components to be greater than 0.7. The probability that a sample of 60 uncorrelated data points has a correlation coefficient greater than 0.7 or less than −0.7 is less than 0.01 and therefore statistically significant, indicating the presence of Alfvénic fluctuations.

[14] Table 2 lists the 153 CIRs observed from the start of 1995 to the end of 2008. The columns from left to right are: event number and time intervals; for the forward boundary, stream interface, reverse boundary, and end of the high speed stream. Also provided are proton density peak, change in solar wind speed across the event, peak in magnetic field strength, peak in total pressure, radial thickness, minimum possible thickness (discussed in section 3.2), meridional, and azimuthal tilts of the CIRs. For non-planar events, the latter three parameters cannot be calculated and are noted with "…".

[15] Out of 153 CIRs, 32 events (20.9%) had shocks identified. Within this group 19 CIRs (12.4%) had forward shocks only, while 13 (8.5%) had reverse shocks only. Comparing planar and non-planar CIRs, we found 12 (16.2%) and 6 (8.1%) planar CIRs with forward and reverse shocks respectively, while there were 7 (8.9%) and 7 (8.9%) non-planar CIRs with forward and reverse shocks respectively. We found no CIRs with both forward and reverse shock pairs.

2.3. Identification of Planar CIRs

[16] We use minimum variance analysis (MVA) to determine the presence of a large scale planar structure from an array of magnetic field vectors [*Sonnerup and Cahill*, 1967].

Table 2. Our List of CIRs[a]

CIR		Forward Boundary		Stream Interface		Reverse Boundary		HSS Boundary		n_p	Δv_p	|B|	P_t	ΔR	ΔW	α	ε
Number	Year	Date	Time	Date	Time	Date	Time	Date	Time	(cm^{-3})	(km s^{-1})	(nT)	(pPa)	(AU)	(AU)	(deg)	(deg)
1[b]	1995	1/1	19:20	2/1	7:53	3/1	18:35	7/1	7:02	40.3	428.5	16.8	159.4	0.55	0.32	41.6 ± 1.1	39.6 ± 0.8
2	1995	28/1	17:55	29/1	7:16	30/1	9:57	4/2	5:48	43.6	475.9	22.8	285.1	0.48	0.32	24.4 ± 0.9	41.9 ± 0.8
3[c]	1995	6/4	12:16	7/4	12:15	7/4	20:21	13/4	1:40	67.8	463.8	29.9	519.8	0.30	…	…	…
4	1995	26/4	12:55	26/4	18:39	27/4	7:28	1/5	4:01	32.1	378.7	18.4	237.9	0.25	…	…	…
5	1995	1/5	20:51	2/5	15:02	2/5	23:53	9/5	9:34	62.0	446.4	17.1	241.8	0.35	0.25	26.0 ± 1.7	36.4 ± 0.8
6	1995	23/5	14:27	23/5	17:08	24/5	4:46	29/5	2:29	23.9	378.3	17.4	212.0	0.18	…	…	…
7[c]	1995	30/5	1:15	30/5	6:13	31/5	4:44	5/6	3:13	26.3	451.5	19.5	216.5	0.40	0.26	27.0 ± 1.4	42.4 ± 0.9
8	1995	18/6	21:23	19/6	8:54	19/6	17:56	24/6	16:04	89.5	448.8	25.4	332.6	0.23	0.19	4.3 ± 1.3	36.4 ± 0.5
9	1995	16/7	9:05	16/7	15:58	17/7	2:30	20/7	19:38	54.3	375.5	21.6	247.7	0.22	0.15	20.9 ± 1.3	41.7 ± 0.8
10	1995	7/8	9:11	7/8	20:42	9/8	3:50	12/8	0:52	35.3	306.2	12.4	128.3	0.51	…	…	…
11	1995	30/10	9:24	30/10	15:46	1/11	8:27	3/11	17:49	32.5	360.6	13.1	104.6	0.48	0.27	−52.5 ± 1.3	18.2 ± 0.6
12[c]	1995	4/11	11:28	5/11	12:43	6/11	0:49	8/11	21:33	26.7	248.2	15.3	168.1	0.41	…	…	…
13[b]	1995	24/12	5:50	24/12	8:57	25/12	22:54	27/12	0:21	77.3	398.1	27.7	499.2	0.57	0.44	−34.8 ± 1.2	21.3 ± 1.1
14[d]	1996	14/1	14:57	14/1	17:20	15/1	3:32	18/1	20:44	38.7	315.6	19.0	244.4	0.17	0.12	37.8 ± 2.3	23.0 ± 1.9
15[b]	1996	18/6	22:34	19/6	1:59	19/6	7:35	22/6	4:43	70.2	175.0	19.8	270.3	0.10	0.10	0.9 ± 2.4	6.6 ± 1.4
16	1996	28/8	16:01	29/8	2:05	29/8	17:50	1/9	3:32	21.5	287.0	13.5	162.2	0.32	…	…	…
17	1996	17/10	5:16	17/10	21:43	18/10	4:15	21/10	17:56	17.2	286.7	13.4	103.5	0.24	…	…	…
18	1996	27/10	7:30	28/10	0:23	28/10	20:53	31/10	19:10	30.0	305.3	14.8	131.1	0.43	0.36	17.5 ± 1.5	27.5 ± 1.3
19	1996	9/12	18:36	9/12	23:38	11/12	6:41	12/12	19:26	47.0	351.3	16.4	158.7	0.46	0.27	−34.8 ± 1.2	43.9 ± 0.7
20	1997	25/1	17:46	26/1	9:17	28/1	8:47	29/1	5:08	27.6	422.6	18.4	212.1	0.73	0.57	37.1 ± 1.2	9.5 ± 0.9
21[b]	1997	16/4	12:17	16/4	23:45	17/4	8:08	20/4	7:45	46.0	209.6	16.7	174.9	0.21	0.20	−9.6 ± 1.6	17.9 ± 1.1
22[b,c]	1997	1/5	11:57	1/5	18:17	1/5	23:49	7/5	15:51	32.3	343.4	16.0	162.7	0.14	0.09	52.8 ± 1.6	7.6 ± 0.7
23[d]	1997	27/6	6:39	27/6	11:55	27/6	15:13	1/7	4:01	36.1	267.2	12.2	108.9	0.09	0.08	4.7 ± 1.9	21.7 ± 1.0
24[e]	1998	15/7	16:23	16/7	2:15	16/7	23:30	20/7	11:48	41.8	357.2	24.4	334.8	0.36	…	…	…
25	1998	22/7	1:17	23/7	0:28	23/7	12:34	26/7	1:49	23.0	390.0	16.6	188.0	0.39	…	…	…
26	1998	6/10	15:24	7/10	9:48	7/10	19:20	14/10	0:21	41.4	331.7	15.0	155.3	0.27	0.23	−2.5 ± 1.1	33.1 ± 0.6
27	1999	5/1	21:39	6/1	13:49	6/1	22:53	12/1	14:06	51.6	233.3	19.8	182.1	0.23	0.18	37.9 ± 1.5	9.6 ± 0.7
28	1999	14/3	10:03	14/3	13:55	14/3	19:28	19/3	11:25	22.9	261.4	12.9	120.3	0.11	…	…	…
29	1999	28/3	17:17	29/3	9:25	30/3	19:43	1/4	12:39	58.9	263.1	15.5	155.6	0.55	0.38	8.9 ± 0.9	45.8 ± 0.7
30	1999	10/4	3:33	10/4	8:28	10/4	19:29	16/4	13:14	32.3	252.3	13.2	130.5	0.18	…	…	…
31[c,e]	1999	24/5	4:27	24/5	20:02	25/5	9:49	29/5	1:31	31.6	221.7	14.7	162.3	0.32	0.24	−3.2 ± 0.9	43.1 ± 0.6
32	1999	8/6	5:58	8/6	19:22	9/6	3:50	14/6	7:39	47.5	355.6	12.8	136.8	0.23	0.15	14.8 ± 0.5	48.6 ± 0.3
33	1999	21/7	13:56	22/7	8:59	22/7	20:09	27/7	18:14	41.1	283.5	19.7	212.1	0.28	…	…	…
34[b]	1999	26/9	14:22	26/9	19:52	27/9	16:04	2/10	22:59	56.6	296.8	19.1	244.2	0.34	…	…	…
35	1999	3/12	2:10	4/12	2:39	4/12	9:44	11/12	15:25	47.5	418.3	21.3	236.0	0.36	0.22	−32.3 ± 1.1	43.7 ± 0.4
36[f]	2000	10/1	4:48	10/1	20:47	11/1	23:04	17/1	20:31	29.8	361.4	22.5	317.8	0.42	…	…	…
37[b,f]	2000	27/1	13:54	27/1	18:57	28/1	8:52	5/2	13:36	132.8	501.4	32.9	677.4	0.27	0.23	18.2 ± 1.2	25.7 ± 1.0
38[b]	2000	5/2	14:49	5/2	21:16	6/2	23:24	11/2	9:30	44.7	336.7	19.7	281.8	0.43	0.38	10.2 ± 1.0	24.7 ± 0.9
39[e]	2000	22/3	10:55	22/3	13:56	22/3	18:06	27/3	23:22	105.4	442.5	23.7	336.5	0.08	…	…	…
40[e]	2000	29/5	14:46	29/5	18:07	30/5	1:24	1/6	11:01	32.9	340.3	20.0	236.7	0.12	0.11	19.7 ± 1.1	12.4 ± 0.9
41	2000	27/8	13:11	28/8	6:53	29/8	3:15	2/9	14:39	23.3	327.2	12.9	123.8	0.44	…	…	…
42	2000	22/10	5:51	22/10	8:45	23/10	5:47	26/10	20:10	32.5	286.7	14.2	121.4	0.29	0.20	19.7 ± 1.6	42.0 ± 1.3
43	2000	6/12	20:07	8/12	0:47	8/12	12:20	14/12	2:19	28.6	376.3	15.2	159.9	0.45	0.32	6.1 ± 1.2	44.2 ± 0.7
44[e,g]	2001	1/6	7:55	1/6	21:28	2/6	11:51	5/6	14:59	74.7	310.8	22.2	261.6	0.26	0.23	13.4 ± 1.1	23.7 ± 0.5
45[b,f]	2001	18/6	1:48	18/6	23:36	20/6	2:57	26/6	12:08	67.0	559.1	20.3	208.1	0.53	…	…	…
46[f]	2001	14/12	15:39	15/12	20:09	16/12	9:29	23/12	7:28	59.6	337.8	25.6	372.2	0.40	…	…	…
47[b]	2001	23/12	22:01	24/12	4:19	24/12	10:49	28/12	8:06	54.1	321.1	23.4	272.9	0.14	0.12	11.5 ± 1.3	23.5 ± 1.1
48	2002	19/1	5:06	20/1	2:07	21/1	5:56	24/1	22:50	48.9	258.0	22.0	256.7	0.51	0.36	−31.7 ± 0.7	35.0 ± 0.5
49	2002	4/2	20:19	5/2	11:29	6/2	2:13	12/2	6:47	44.6	410.2	20.5	272.0	0.31	…	…	…
50	2002	3/3	13:38	4/3	15:32	5/3	4:54	11/3	23:48	48.4	432.2	21.5	286.6	0.43	…	…	…
51[b]	2002	29/3	21:39	30/3	6:30	31/3	15:12	4/4	17:47	61.8	516.8	23.4	297.7	0.57	…	…	…
52[f]	2002	18/6	21:10	19/6	4:26	19/6	13:55	25/6	23:49	41.6	221.7	16.6	179.0	0.18	…	…	…
53	2002	4/7	14:26	5/7	12:07	6/7	11:46	10/7	7:03	45.2	292.0	15.6	205.8	0.43	0.28	16.2 ± 1.0	46.9 ± 0.7
54	2002	23/10	13:20	24/10	9:59	24/10	20:57	29/10	10:26	37.7	409.6	16.7	180.5	0.40	0.23	−14.7 ± 1.3	52.8 ± 1.3
55[b,g]	2002	20/11	10:16	21/11	5:11	21/11	12:20	26/11	2:52	77.8	445.3	37.3	784.4	0.31	0.29	20.5 ± 1.0	9.7 ± 0.8
56[f]	2002	6/12	8:08	7/12	7:42	7/12	17:00	13/12	5:59	42.3	362.5	19.1	246.0	0.36	…	…	…
57[e]	2002	14/12	2:29	14/12	14:04	15/12	0:36	17/12	17:32	24.3	265.6	15.4	158.2	0.23	…	…	…
58	2002	26/12	8:15	27/12	0:08	27/12	12:13	31/12	12:09	20.9	445.2	18.2	211.2	0.36	…	…	…
59	2003	2/1	19:25	3/1	10:02	4/1	2:02	7/1	10:30	55.8	298.0	15.8	198.5	0.36	0.24	−35.6 ± 0.9	35.6 ± 0.5
60[c,e]	2003	26/2	19:24	27/2	0:41	27/2	13:29	2/3	15:03	41.3	239.6	18.4	202.3	0.23	0.22	6.1 ± 1.6	−10.9 ± 1.0
61	2003	3/3	1:44	3/3	22:42	4/3	9:54	11/3	17:20	20.7	306.3	16.4	155.4	0.34	…	…	…
62[e]	2003	26/7	12:04	26/7	19:21	27/7	4:39	3/8	20:10	68.4	567.5	36.6	606.1	0.20	…	…	…
63[g]	2003	20/8	6:24	21/8	0:22	21/8	22:06	29/8	4:58	24.2	464.5	16.6	189.2	0.51	…	…	…
64	2003	16/9	9:05	17/9	0:44	17/9	15:59	23/9	12:35	34.8	488.2	24.1	281.2	0.42	…	…	…
65	2003	13/10	6:33	14/10	18:28	15/10	2:23	22/10	3:04	133.0	475.9	22.5	681.5	0.50	…	…	…
66[b]	2003	7/12	13:46	8/12	11:35	10/12	11:44	18/12	7:11	17.3	496.0	17.3	154.4	1.00	…	…	…
67	2003	19/12	23:35	20/12	10:45	21/12	20:24	30/12	23:53	37.2	363.5	22.6	274.5	0.50	…	…	…
68[h]	2004	11/2	9:19	12/2	1:42	12/2	10:33	20/2	17:58	44.8	467.8	21.9	250.2	0.29	0.19	20.7 ± 0.7	45.1 ± 0.5
69[c,e]	2004	8/3	10:50	9/3	14:53	10/3	7:23	16/3	17:51	24.3	481.4	18.3	182.5	0.50	0.34	−10.9 ± 1.0	46.0 ± 0.4

Table 2. (continued)

CIR		Forward Boundary		Stream Interface		Reverse Boundary		HSS Boundary		n_p	Δv_p	|B|	P_t	ΔR	ΔW	α	ε
Number	Year	Date	Time	Date	Time	Date	Time	Date	Time	(cm^{-3})	(km s^{-1})	(nT)	(pPa)	(AU)	(AU)	(deg)	(deg)
70	2004	28/6	4:19	28/6	18:43	29/6	8:30	3/7	6:11	33.0	279.4	17.8	193.2	0.29	0.23	26.4 ± 1.0	27.3 ± 0.9
71	2004	19/11	13:21	20/11	16:39	21/11	0:57	22/11	11:14	60.0	303.8	17.7	203.1	0.39	0.25	24.2 ± 0.8	45.7 ± 0.6
72[c]	2004	28/11	18:07	29/11	6:54	30/11	12:15	2/12	18:29	25.9	330.4	18.1	168.2	0.54	…	…	…
73	2004	15/12	21:18	16/12	18:57	17/12	16:06	20/12	20:40	25.4	339.9	14.8	157.5	0.53	…	…	…
74	2005	1/1	10:12	2/1	2:49	2/1	9:40	7/1	13:18	39.6	438.3	18.2	187.7	0.32	…	…	…
75	2005	11/1	19:52	12/1	3:03	12/1	15:46	16/1	12:20	40.8	381.9	21.5	302.3	0.26	0.22	−1.2 ± 1.7	30.7 ± 1.1
76	2005	6/2	3:10	7/2	13:32	8/2	18:06	11/2	19:40	34.5	473.7	18.2	178.0	0.80	…	…	…
77	2005	5/3	3:02	6/3	7:55	7/3	18:13	11/3	12:53	47.6	440.8	17.9	176.4	0.79	…	…	…
78[e]	2005	24/3	6:55	24/3	13:00	25/3	16:58	29/3	3:23	37.4	431.0	18.2	187.5	0.35	…	…	…
79[e]	2005	3/4	15:43	4/4	5:26	5/4	3:00	6/4	13:52	34.7	377.3	16.6	210.0	0.39	0.29	−30.3 ± 0.9	31.5 ± 0.6
80[i]	2005	19/4	20:10	20/4	2:26	20/4	12:57	26/4	15:59	53.3	276.4	17.6	234.9	0.19	0.16	14.1 ± 1.3	31.4 ± 0.7
81	2005	29/4	15:02	30/4	4:10	1/5	7:34	3/5	18:22	62.2	406.8	16.5	189.6	0.51	…	…	…
82	2005	4/6	10:07	4/6	16:11	5/6	12:08	10/6	15:08	43.5	358.9	16.5	177.9	0.33	0.26	−12.3 ± 1.4	34.2 ± 1.1
83	2005	23/6	1:57	23/6	9:17	25/6	8:19	27/6	15:08	104.2	370.4	23.6	362.4	0.61	0.56	19.6 ± 0.6	14.3 ± 0.5
84	2005	1/7	1:18	1/7	17:31	2/7	7:10	7/7	1:27	46.6	296.3	17.6	211.9	0.33	…	…	…
85[g]	2005	19/7	19:28	20/7	11:50	21/7	7:01	23/7	10:56	22.3	294.6	14.0	128.8	0.42	…	…	…
86[b]	2005	27/7	18:47	28/7	7:49	29/7	13:50	1/8	16:40	42.0	312.1	16.6	174.3	0.54	0.38	33.9 ± 1.1	32.5 ± 0.7
87	2005	15/8	6:22	15/8	18:05	17/8	0:03	19/8	18:16	25.0	381.2	13.9	117.8	0.54	…	…	…
88[e]	2005	7/10	3:28	8/10	1:38	8/10	6:43	11/10	23:26	65.7	452.8	27.9	399.8	0.27	…	…	…
89	2005	24/10	17:33	25/10	2:40	26/10	14:13	28/10	14:04	50.2	268.3	12.9	171.6	0.45	…	…	…
90	2005	2/11	14:57	2/11	19:41	4/11	10:12	8/11	16:53	41.6	371.5	18.1	191.2	0.63	…	…	…
91	2005	29/11	16:38	29/11	22:35	2/12	2:26	4/12	23:38	28.0	394.8	16.6	159.5	0.89	…	…	…
92[i]	2005	18/12	20:20	19/12	15:58	20/12	10:03	22/12	21:10	52.7	387.0	15.6	144.0	0.36	0.26	−7.0 ± 1.3	43.6 ± 0.5
93	2005	27/12	7:14	27/12	14:20	28/12	0:52	30/12	23:21	53.7	424.7	21.7	327.5	0.21	…	…	…
94	2006	18/2	17:53	20/2	9:41	21/2	13:18	26/2	14:05	37.8	385.6	11.9	108.7	0.74	…	…	…
95[d]	2006	9/3	10:24	10/3	3:52	11/3	1:19	12/3	8:16	33.8	246.3	13.7	132.3	0.39	…	…	…
96	2006	18/3	5:23	18/3	21:12	20/3	5:32	22/3	11:29	33.9	372.7	14.2	139.2	0.68	…	…	…
97	2006	8/4	10:22	9/4	9:48	9/4	22:30	13/4	2:04	25.1	414.3	19.5	228.5	0.39	…	…	…
98	2006	21/4	8:08	21/4	15:14	22/4	15:45	25/4	22:28	44.0	284.7	13.7	129.5	0.34	…	…	…
99	2006	6/5	10:59	6/5	16:09	7/5	7:01	9/5	9:23	65.2	331.4	18.7	253.5	0.24	0.21	−17.8 ± 1.7	20.9 ± 1.0
100	2006	17/5	10:51	18/5	10:22	18/5	15:14	24/5	8:06	36.8	326.8	16.6	181.3	0.25	…	…	…
101	2006	6/6	3:56	6/6	11:11	7/6	9:35	12/6	16:29	56.9	366.4	15.8	183.4	0.35	0.23	17.3 ± 1.1	47.8 ± 0.6
102	2006	27/6	0:50	28/6	6:56	29/6	5:34	3/7	7:48	34.8	358.0	14.5	126.8	0.52	0.29	−23.0 ± 0.7	52.9 ± 0.7
103	2006	3/7	22:17	4/7	13:00	5/7	8:05	8/7	17:42	82.7	377.5	19.8	236.2	0.36	0.23	−12.5 ± 0.9	49.4 ± 0.4
104	2006	27/7	12:51	27/7	20:55	28/7	10:58	29/7	19:02	31.6	371.2	15.5	210.1	0.27	…	…	…
105	2006	30/7	22:30	31/7	9:02	1/8	11:09	4/8	3:39	29.9	286.9	15.8	168.0	0.44	0.34	−24.7 ± 1.2	31.8 ± 0.7
106	2006	6/8	23:13	7/8	4:18	7/8	19:32	12/8	16:21	59.8	335.1	20.9	310.0	0.24	…	…	…
107[d]	2006	26/8	23:59	27/8	11:47	28/8	2:45	30/8	22:36	56.9	403.5	21.4	305.0	0.28	0.24	−5.9 ± 0.8	31.7 ± 0.7
108	2006	3/9	23:34	4/9	3:57	4/9	20:11	8/9	1:38	25.3	249.5	15.3	162.9	0.26	…	…	…
109[e]	2006	23/9	11:39	24/9	2:42	24/9	6:10	28/9	20:01	83.3	373.5	20.8	450.9	0.18	…	…	…
110	2006	7/10	10:34	7/10	15:02	7/10	19:56	11/10	0:12	45.1	235.6	15.1	149.0	0.09	0.08	11.8 ± 1.1	23.7 ± 0.7
111	2006	19/10	23:18	20/10	18:36	21/10	0:18	24/10	19:56	56.3	376.2	19.4	210.2	0.25	0.18	32.2 ± 1.1	30.9 ± 0.8
112	2006	27/10	18:03	28/10	19:32	29/10	3:27	31/10	11:14	42.6	318.3	13.8	112.1	0.32	…	…	…
113	2006	9/11	11:50	10/11	0:41	10/11	10:26	13/11	0:50	57.1	370.0	19.6	245.1	0.24	0.19	−31.5 ± 0.6	21.1 ± 0.6
114[c]	2006	22/11	7:54	23/11	8:27	24/11	7:19	28/11	11:49	32.1	349.1	17.7	165.8	0.49	…	…	…
115[g]	2006	18/12	9:19	18/12	18:06	21/12	3:43	26/12	11:18	32.0	379.3	12.3	103.7	0.93	…	…	…
116	2007	28/1	13:31	29/1	8:23	29/1	20:23	4/2	18:17	66.0	422.8	20.9	255.5	0.32	0.24	−2.8 ± 0.7	41.2 ± 0.5
117[d]	2007	12/2	8:58	12/2	22:33	14/2	10:28	21/2	10:07	61.4	462.3	16.3	198.6	0.63	…	…	…
118	2007	27/2	0:57	27/2	15:29	28/2	11:00	2/3	13:07	26.6	339.2	17.3	146.0	0.42	…	…	…
119	2007	11/3	6:56	11/3	23:02	14/3	3:59	17/3	20:06	49.3	428.4	12.4	126.5	0.89	…	…	…
120	2007	31/3	20:33	1/4	11:34	2/4	10:58	5/4	18:01	44.6	331.1	14.4	136.3	0.48	0.44	−1.5 ± 0.9	24.6 ± 0.7
121[b]	2007	7/5	7:23	7/5	13:06	8/5	2:38	11/5	10:33	73.5	391.6	21.7	220.6	0.22	0.18	11.7 ± 1.0	29.0 ± 0.8
122	2007	17/5	20:26	18/5	10:41	19/5	6:12	21/5	17:00	60.7	375.9	20.4	260.1	0.39	0.29	−4.2 ± 0.9	40.3 ± 0.5
123[c]	2007	13/6	3:40	13/6	19:48	14/6	22:02	20/6	16:48	25.9	351.7	11.7	97.0	0.41	…	…	…
124[i]	2007	21/6	7:12	21/6	9:13	23/6	2:08	23/6	17:26	35.6	226.4	11.8	103.0	0.52	…	…	…
125	2007	29/6	13:07	29/6	17:23	30/6	3:38	3/7	9:07	56.9	235.0	15.6	147.7	0.16	0.06	52.5 ± 1.1	47.2 ± 0.9
126	2007	3/7	8:59	3/7	22:07	4/7	5:30	8/7	10:15	22.9	315.7	16.0	155.3	0.21	0.17	9.3 ± 1.7	37.3 ± 1.1
127	2007	10/7	16:38	11/7	1:17	11/7	11:03	13/7	4:37	81.2	302.3	19.9	249.5	0.19	0.16	−4.0 ± 0.7	36.6 ± 0.5
128	2007	20/7	3:37	20/7	11:31	21/7	3:20	23/7	21:28	66.2	255.4	13.3	175.7	0.23	0.17	31.4 ± 1.2	31.7 ± 0.9
129	2007	28/7	19:31	29/7	2:37	1/8	14:15	4/8	0:38	46.6	323.8	17.3	164.3	1.16	…	…	…
130	2007	6/8	5:23	6/8	16:05	7/8	7:36	8/8	11:42	28.2	430.3	18.3	199.9	0.29	…	…	…
131	2007	10/8	6:57	10/8	14:16	11/8	2:48	13/8	3:41	27.8	233.1	15.2	143.1	0.23	…	…	…
132	2007	26/8	8:31	26/8	16:56	27/8	0:47	29/8	0:23	69.5	345.0	21.4	230.5	0.16	0.12	33.4 ± 0.8	24.4 ± 0.6
133[b]	2007	27/9	10:55	27/9	18:42	29/9	3:40	5/10	23:47	36.3	343.1	14.3	139.5	0.53	…	…	…
134[d,i]	2007	17/10	21:45	18/10	18:52	19/10	13:45	22/10	14:25	20.8	392.6	14.7	125.4	0.47	0.36	32.4 ± 0.9	25.6 ± 0.7
135[b]	2007	25/10	10:41	25/10	14:11	25/10	19:15	30/10	7:07	36.6	374.1	20.8	222.1	0.11	…	…	…
136	2007	10/12	5:22	11/12	0:56	12/12	0:47	15/12	2:49	28.7	354.4	17.3	201.5	0.53	…	…	…
137[b]	2007	17/12	1:59	17/12	7:21	20/12	21:48	24/12	4:07	65.7	412.7	19.4	253.6	1.33	…	…	…
138	2008	9/2	17:36	10/2	6:32	11/2	8:39	18/2	6:21	29.5	376.3	17.2	182.7	0.52	…	…	…

Table 2. (continued)

CIR Number	Year	Forward Boundary Date	Forward Boundary Time	Stream Interface Date	Stream Interface Time	Reverse Boundary Date	Reverse Boundary Time	HSS Boundary Date	HSS Boundary Time	n_p (cm^{-3})	Δv_p (km s^{-1})	|B| (nT)	P_t (pPa)	ΔR (AU)	ΔW (AU)	α (deg)	ε (deg)
139	2008	27/2	13:44	28/2	19:43	1/3	8:50	3/3	19:49	36.2	488.5	11.6	105.4	0.93	…	…	…
140	2008	8/3	4:57	8/3	17:26	9/3	12:16	16/3	13:21	49.7	408.6	17.9	201.8	0.34	…	…	…
141	2008	26/3	2:16	26/3	12:16	28/3	6:07	31/3	9:41	33.7	332.2	11.5	100.9	0.71	…	…	…
142	2008	3/4	20:03	4/4	19:40	6/4	3:53	13/4	8:08	20.6	442.2	14.5	133.1	0.70	…	…	…
143[c]	2008	15/4	16:32	16/4	10:42	16/4	19:46	21/4	16:20	26.4	269.6	13.4	136.7	0.28	0.18	50.9 ± 0.8	8.8 ± 0.8
144	2008	22/4	17:22	23/4	5:13	24/4	10:44	30/4	1:06	22.8	348.9	15.3	135.1	0.52	…	…	…
145	2008	14/6	11:16	14/6	16:42	15/6	20:48	18/6	20:50	45.2	484.6	18.4	205.3	0.43	0.29	-2.3 ± 1.1	47.4 ± 0.8
146[b]	2008	24/6	19:08	25/6	17:01	26/6	17:30	30/6	6:50	25.2	365.9	15.1	113.9	0.53	0.38	31.9 ± 1.1	31.3 ± 0.8
147	2008	11/7	1:06	11/7	22:33	12/7	10:35	17/7	19:43	20.2	394.0	15.3	122.9	0.35	0.28	-8.3 ± 0.8	35.0 ± 0.5
148	2008	8/8	19:48	9/8	6:08	10/8	3:52	13/8	8:56	41.9	330.9	20.1	238.6	0.40	0.34	-28.7 ± 1.0	8.9 ± 0.6
149	2008	2/9	22:41	3/9	7:34	4/9	11:36	10/9	5:51	32.8	348.2	15.5	137.4	0.39	0.39	8.4 ± 0.8	3.8 ± 0.7
150[f]	2008	14/9	4:42	15/9	4:51	15/9	11:47	20/9	2:10	63.6	339.2	15.9	195.3	0.27	0.23	21.9 ± 1.0	25.3 ± 0.8
151[d]	2008	28/10	3:08	28/10	20:45	29/10	13:29	4/11	2:47	21.6	440.7	14.0	113.6	0.40	…	…	…
152[d]	2008	6/11	13:40	7/11	17:30	8/11	5:31	12/11	14:10	36.1	315.0	13.9	138.2	0.37	0.27	20.4 ± 1.1	37.8 ± 0.6
153	2008	24/11	22:33	25/11	3:59	25/11	10:30	30/11	6:03	95.8	403.4	24.3	334.1	0.12	0.11	11.3 ± 1.0	18.6 ± 0.7

[a]From left to right, the table lists the CIR number, start date and time, stream interface date and time, end date and time, end of the high speed stream date and time, peak in proton density, change in solar wind speed, magnetic field strength peak, total pressure peak, radial width, minimum width, CIR meridional tilt angle and CIR azimuthal tilt angle.
[b]Forward shock present.
[c]Possible ICME ahead of event.
[d]Data gap ahead of event.
[e]Reverse shock present.
[f]Possible ICME behind event.
[g]Definite ICME ahead of event.
[h]Definite ICME behind event.
[i]Data gap during event.

We calculate the covariance matrix for an array of vectors, representing the magnetic field measurements across the CIR. We define the covariance matrix as:

$$M^B_{\mu\theta} = \langle B_\mu B_\theta \rangle - \langle B_\mu \rangle \langle B_\theta \rangle \quad (1)$$

where μ and θ describe arbitrary components of the magnetic field vector. We then calculate eigenvalues and eigenvectors for the covariance matrix. The eigenvalues, λ_i, represent the physical scalar values of maximum, minimum, and intermediate variance. The corresponding eigenvectors, $\mathbf{x_i}$, represent the directions of these three variances in the original coordinate system of the magnetic field. These unit vectors are also orthogonal to each other. By selecting the eigenvector corresponding to the minimum variance we identify the normal to a plane.

[17] To verify that a CIR can be approximated by a plane, we use the following three requirements: (1) $\lambda_{Int.}/\lambda_{Min.} \geq 2.5$, (2) $\langle B_N/|B| \rangle \leq 0.2$, and (3) uncertainty, σ, in α and ε should be less than 5° [*Clack et al.*, 2000; *Neugebauer et al.*, 1993; *Paschmann and Daly*, 1998]. Prerequisites (1) and (2) eliminate events that have spatially degenerate data ellipsoids, which are not well approximated as planar. The uncertainty in α and ε is determined using the technique developed by *Khrabrov and Sonnerup* [1998]. We found 74 CIRs (48.4%) in Table 2 satisfied the above conditions.

[18] Table 3 estimates the validity of using the above requirements to define planarity. The table shows the number of events that are defined as planar by the current requirements and for values shifted by ±50%. The number of events classified as planar is most sensitive to changes in the ratio of intermediate to minimum eigenvalues (criterion #1), while the requirement that $\Delta\alpha$ and $\Delta\varepsilon$ be less than 5° (criterion #3) least affects the number of identified planar events.

[19] After identifying the anti-Sunward normal vector of the planar magnetic structure, we transform it into a spherical coordinate system with its magnitude equal to 1. In our analysis, the magnetic field is defined in the RTN coordinate system. We use the same coordinates in our definition of the meridional tilt, $\alpha = \arcsin(n_N/|\mathbf{n}|)$, and azimuthal tilt, $\varepsilon = \arctan(n_T/n_R)$, as shown in Figure 1.

[20] Figure 3 compares two CIRs from our list: a planar magnetic structure represented as a cylindrical projection of magnetic latitude and longitude (Figure 3a) and on the surface of a sphere (Figure 3b), while Figures 3d and 3e show a CIR from our list that was considered non-planar.

Table 3. Properties Required of Each Event to Be Considered a Good Candidate for MVA and Therefore to Be Approximated as a PMS[a]

Current Requirement	Number of Events	± 50% Change	Variation in Number of Events
$\lambda_{Int.}/\lambda_{Min.} \geq 2.5$	85	1.25	151 (+66)
		3.75	34 (−51)
$\mathbf{B}\cdot\mathbf{n} \leq 0.2$	127	0.3	141 (+14)
		0.1	104 (−13)
$\Delta\alpha, \Delta\varepsilon < 5°$	148	7.5	151 (+3)
		2.5	138 (−10)

[a]From left to right the table shows requirements used in this study, the number of CIRs from our list that each requirement identified as planar, the 50% increase and decrease of each of these requirements and in the fourth column we show the number of planar events found by the high and low values of each requirement.

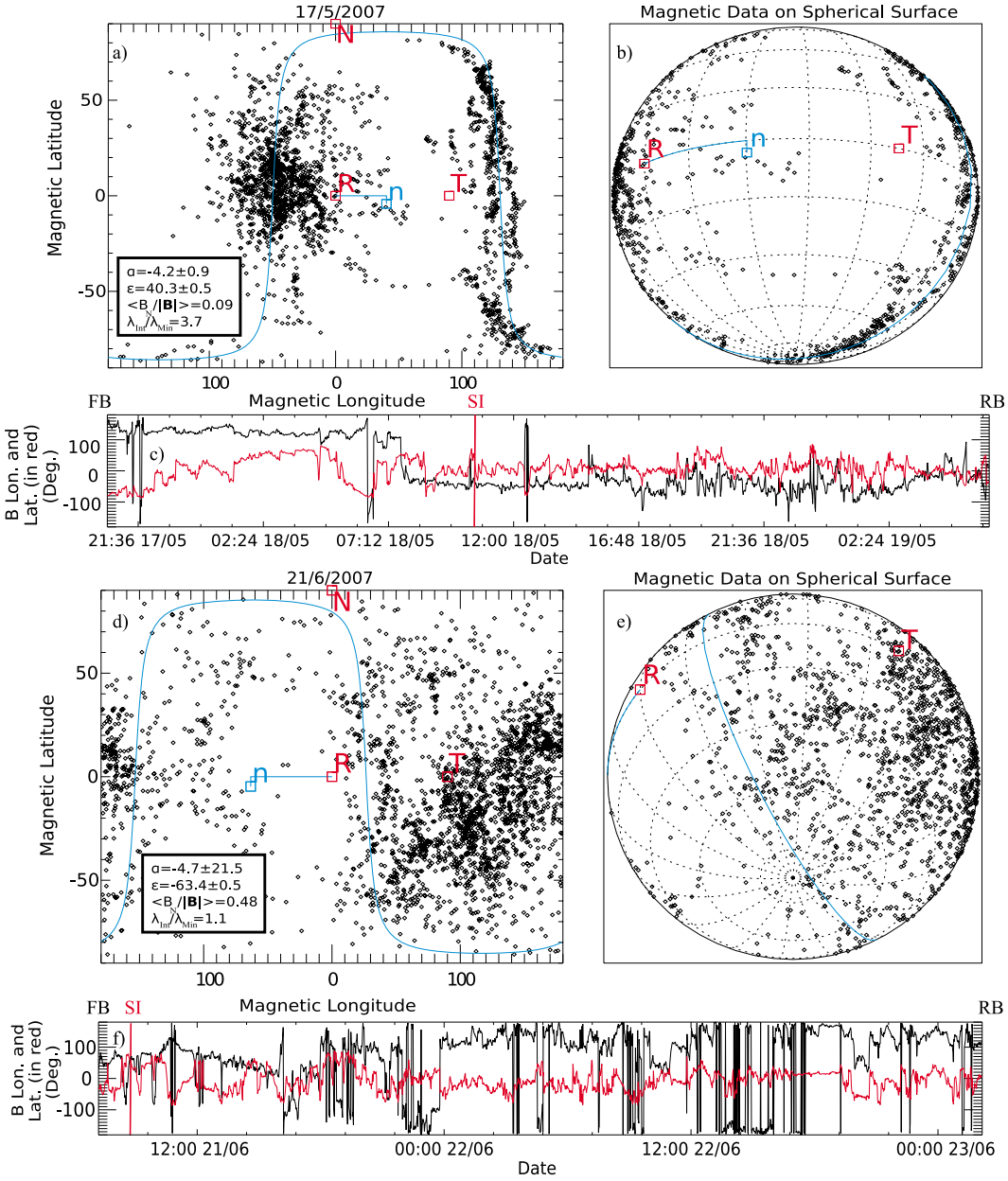

Figure 3. Magnetic field vector data from two CIRs on our list (CIRs # 122 and 124 in Table 2). (a, d) Black data points represent the magnetic latitude and longitude in a cylindrical map. (b, e) The same data as Figures 3a and 3c, but mapped onto the surface of a sphere. Each panel includes the RTN axis (red dots), the normal vector to the plane (blue square) and the angles α and ε (blue curves connecting the radial unit vector to the normal vector). The blue sinusoidal pattern in Figures 3a and 3d, and great circle in Figures 3b and 3e, both represent the position of the plane determined through MVA. (c and f) All of the magnetic latitude and longitude data used in time-series, with vertical lines marking the location of the forward boundary, stream interface, and reverse boundary.

The planar event met all criteria with $\Delta\alpha = 1.3°$, $\Delta\varepsilon = 0.8°$, $\langle \mathbf{B}_N/|B| \rangle = 0.017$ and $\lambda_{Int.}/\lambda_{Min.} = 4.8$. The non-planar event was rejected because it failed to meet all three conditions described above; it had $\Delta\alpha = 21.5°$, $\Delta\varepsilon = 2.35°$, $\langle \mathbf{B}_N/|B| \rangle = 0.48$ and $\lambda_{Int.}/\lambda_{Min.} = 1.06$. Figures 3c and 3f show the time series of the magnetic longitude (black) and latitude (red) for the two events, with the forward boundary (FB), reverse boundary (RB), and stream interface (SI) locations shown as vertical lines.

[21] A great circle is the bisection of a sphere with a plane, which we show in Figures 3a, 3b, 3d, and 3e as a blue curve. In a cylindrical projection, a great circle traces a wave like pattern along the abscissa. The same pattern can also be derived by using the assumption $\mathbf{B}\cdot\mathbf{n} = 0$, where $\mathbf{n}$ is the unit vector normal to the plane and $\mathbf{B}$ is the magnetic field vector.

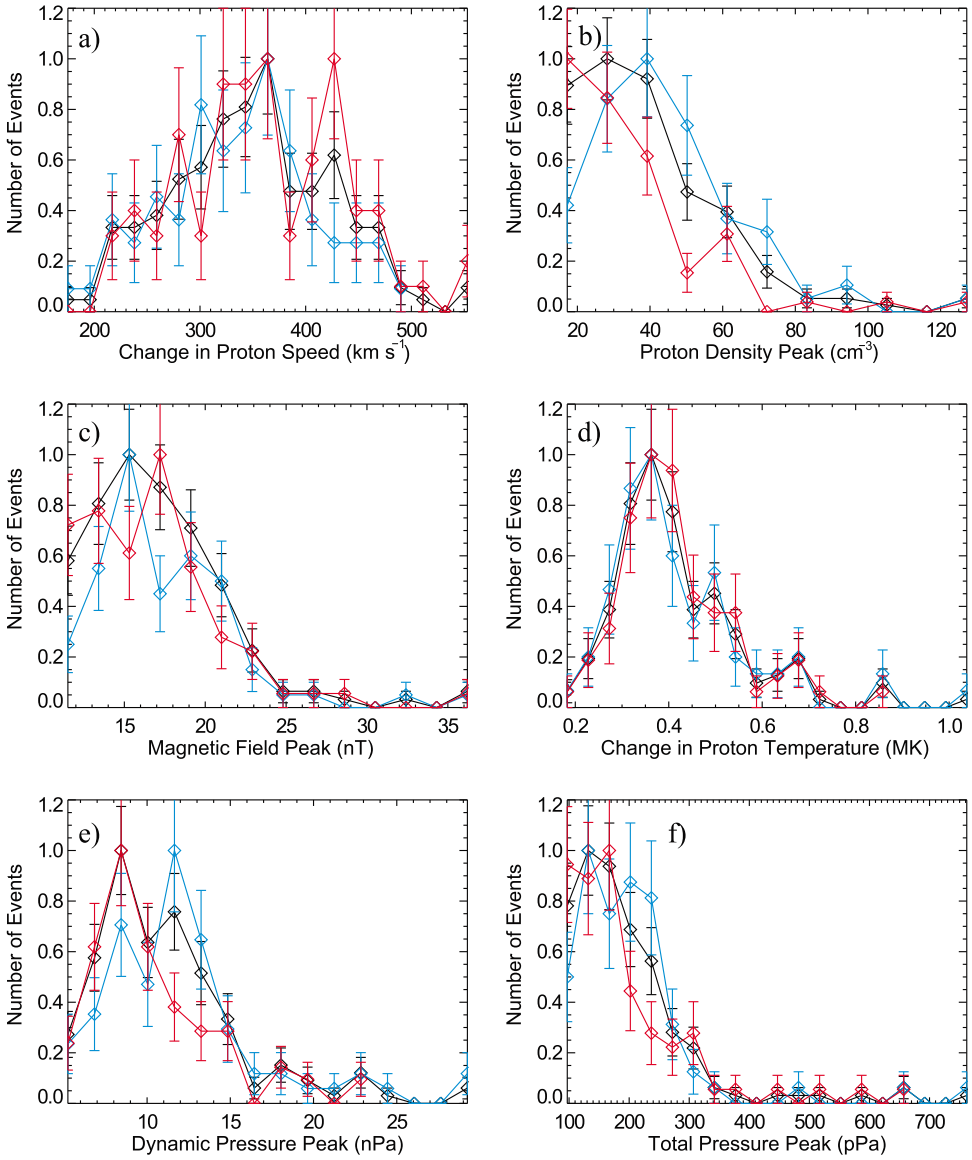

Figure 4. Normalized distributions of CIR properties grouped as planar (blue), non-planar (red) and all (black) CIRs from Table 2. Listed here are (a) change in solar wind speed, (b) peak proton density, (c) peak magnetic field strength, (d) change in proton temperature, (e) peak in dynamic pressure, and (f) peak in total pressure.

Resolving **B** and **n** into their components and converting to a spherical coordinate system in which θ and φ represent magnetic latitude and longitude, yields equation (2) [*Jones et al.*, 1999].

$$\tan\theta = -\left(\frac{n_R\cos\varphi + n_T\sin\varphi}{n_N}\right) \tag{2}$$

3. Results

3.1. Bulk Plasma and Magnetic Field Properties of CIRs

[22] Figure 4 shows the distribution of six CIR properties: the change in solar wind speed across the CIR (Figure 4a), peak in proton density (Figure 4b), magnetic field strength peak (Figure 4c), change in solar wind temperature across the event (Figure 4d), peak in dynamic pressure (Figure 4e), and peak in total pressure (Figure 4f). We have divided the events into three groups: all (153 CIRs; black curve), planar (74 CIRs; blue curve), and non-planar (79 CIRs; red curve) CIRs. Each histogram is normalized to its corresponding maximum value. Error bars show the normalized standard deviation of each bin, assuming Poisson statistics.

[23] For each distribution we have also performed a statistical analysis. Table 4 shows the medians, means, and standard deviations for the properties shown in Figure 4, and are divided into groups of planar, non-planar, and all CIRs. After comparing the means and standard deviations

Table 4. The Median, Mean, and Standard Deviation of Planar, Non-planar, and All CIR Properties Shown in Figure 3

	Δv_p (km s^{-1})	n_p (cm^{-3})	|B| (nT)	ΔT_p (MK)	$P_{Dyn.}$ (nPa)	P_t (pPa)
Median						
All	359.6	41.3	17.3	0.408	19.4	188.0
Planar	351.3	45.2	17.7	0.406	19.1	203.1
Non-planar	371.5	35.3	17.3	0.410	19.4	181.3
Mean						
All	359.7	44.8	18.0	0.440	19.8	214.2
Planar	347.8	50.1	18.4	0.442	19.7	220.4
Non-planar	370.9	39.9	17.6	0.437	19.8	208.5
Standard deviation						
All	75.6	20.7	4.4	0.138	5.6	108.8
Planar	71.2	20.7	4.3	0.153	5.7	109.4
Non-planar	78.2	19.5	4.5	0.123	5.5	108.7

of each parameter, we note that there is no statistical difference between the properties of planar and non-planar CIRs, as can also be seen from the histograms shown in Figure 4.

[24] Figure 5 shows scatterplots of: peak in magnetic field strength versus proton density (Figure 5a), magnetic field strength peak versus the change in solar wind speed (Figure 5b), peaks in magnetic versus thermal pressure

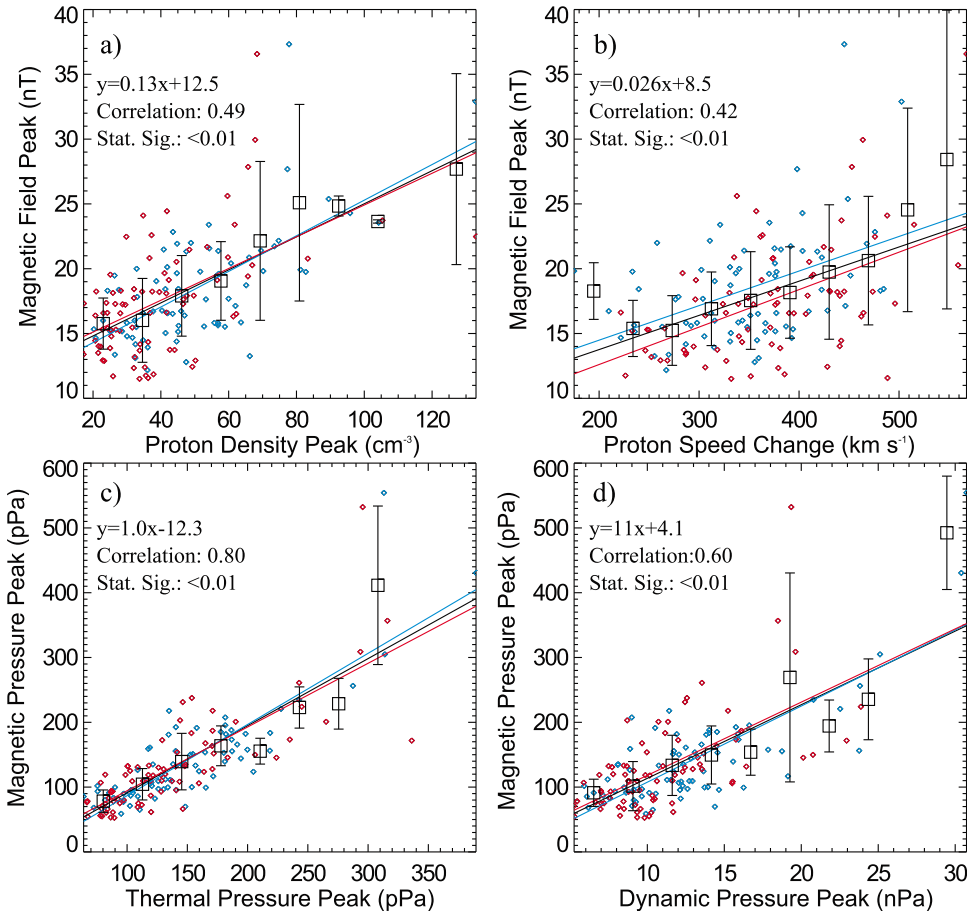

Figure 5. Scatterplots of (a) the peaks in magnetic field strength and proton density, (b) peak in magnetic field strength and change in solar wind speed, (c) peaks in magnetic and thermal pressure, and (d) peaks in magnetic and dynamic pressure. Linear fits are shown for planar (blue), non-planar (red), and all CIRs (black). The black squares with error bars show the mean and standard deviation of the ordinate divided into 10 bins along the abscissa. Within each panel the linear equation of fit, correlation coefficient, and statistical significance is shown for all CIRs.

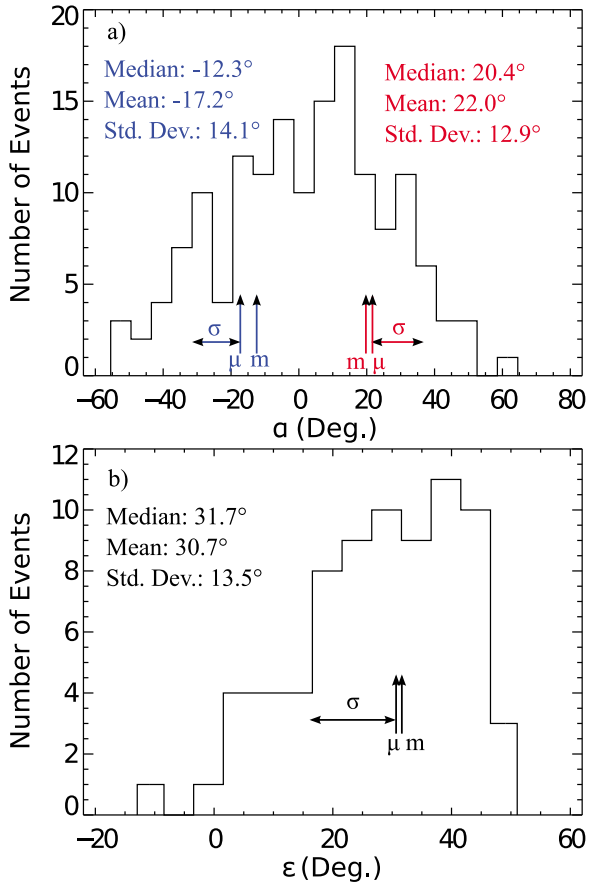

Figure 6. Histograms of (a) the meridional tilt, α, and (b) azimuthal tilt, ε, for planar CIRs within our list. Arrows indicate the median, mean and standard deviations of the corresponding distributions.

(Figure 5c), and peaks in magnetic versus dynamic pressure (Figure 5d). The strongest correlations occur between the different types of pressure (Figures 5c and 5d). In contrast Figures 5a and 5b show a weaker relationship between |**B**| and n_p and also between |**B**| and v_p. Finally we note that the linear fits for planar and non-planar CIRs are remarkably similar.

3.2. Tilt and Thickness of CIRs

[25] Figure 6 shows the distributions of the meridional tilt out of the ecliptic, α (Figure 6a) and the azimuthal tilt, ε describing the three dimensional orientation of each planar CIR (Figure 6b). Also provided are the medians (m), means (μ), and standard deviations (σ) for the azimuthal tilt (black) as well as the northern (red) and southern (blue) tilt in the meridional direction.

[26] Figure 6 shows several interesting results. (1) The average azimuthal tilt is 30.7 ± 13.5°. (2) The average positive meridional tilt is 22.0 ± 12.9°, and −17.2 ± 14.1° for negative values. (3) 45 of 73 planar CIRs (61.6%) have northern tilt. Note that σ for a binomial distribution for 74 CIRs with northern and southern tilts equally likely to occur is 4.3, which makes the occurrence of 16 more CIRs with northern tilt statistically significant.

[27] We determine the thickness of each planar CIR using two different methods. First, we measure the distance from the forward boundary to the reverse boundary along the anti-Sunward vector, ΔR (equation (3)), and second, we estimate a lower limit for the distance between the forward and reverse boundaries, Δx (equation (4)), using the inferred values of α and ε.

$$\Delta R = \langle v_p \rangle * (t_f - t_s) \tag{3}$$

$$\Delta x = \langle v_p \rangle * (t_f - t_s) * \cos\alpha * \cos\varepsilon = \Delta R * \cos\alpha * \cos\varepsilon \tag{4}$$

We calculate the average proton speed, $\langle v_p \rangle$ as the mean solar wind speed between the forward and reverse boundary. The exact time of passage for the forward and reverse boundary are defined as t_s and t_f respectively.

[28] Figure 7a compares the distributions of ΔR (red) and Δx (black). Figure 7b shows a scatterplot of the radial (ΔR) and minimum (Δx) widths, for all 73 planar events in our survey. The red curve in Figure 7b has a slope of 1, data points have larger radial widths than the red curve if α or ε

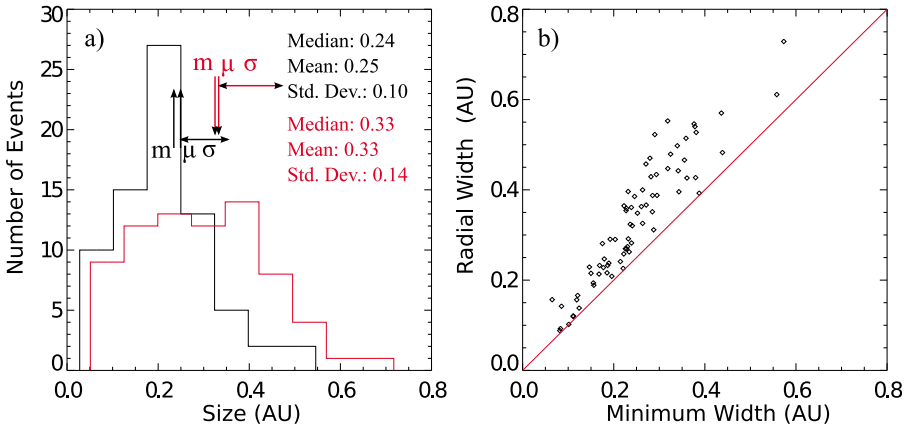

Figure 7. (a) Distributions of radial (red) and minimum (black) widths. (b) Scatterplots of the radial and minimum widths for each event, the red curve shows the relationship of radial to minimum widths if the meridional, α and azimuthal, ε tilt is 0.

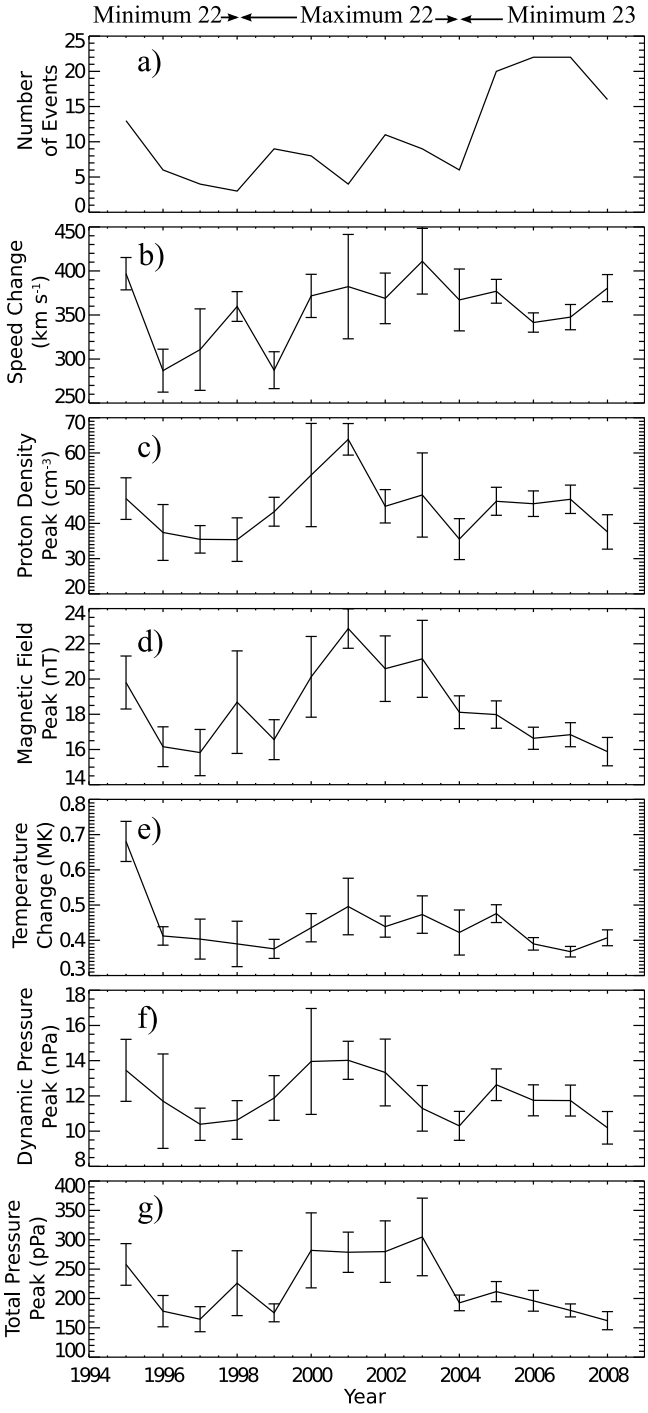

Figure 8. (a) Annual variation of number of CIRs, (b) change in solar wind speed, (c) proton density peak, (d) magnetic field strength peak, (e) change in proton temperature, (f) dynamic pressure peak, and (g) total pressure. The annual mean is shown for each year, while the error bars show the uncertainty in the mean.

are non-zero. Figure 7 shows a mean minimum width of 0.25 AU with a standard deviation of 0.10 AU. We also see that the mean radial width is 0.33 AU with a standard deviation of 0.14 AU.

3.3. Variation of Bulk Plasma Properties, Magnetic Field Properties, and Tilt Over Solar Cycle

[29] We now examine CIR properties as a function of solar cycle. Figure 8 shows the annual occurrence frequency of CIRs (Figure 8a), change in solar wind speed (Figure 8b), peak in proton density (Figure 8c), peak in magnetic field strength (Figure 8d), change in solar wind temperature (Figure 8e), peak in dynamic pressure (Figure 8f), and peak in total pressure (Figure 8g). Data points indicate the mean for each year and the error bars represent the uncertainty in the mean.

[30] The annual variations of CIR properties reveal several interesting results. (1) The decline to solar minimum 23, from 2005 to 2008, shows a notable increase in CIR occurrence. (2) The strongest compression within CIRs occur during solar maximum, from 1999 to 2002, as is evident from the peaks in proton density, magnetic field strength, dynamic pressure and total pressure (Figures 8c, 8d, 8f, and 8g). (3) CIRs in 1995 have notably higher proton temperatures. Upon more detailed inspection, we found that CIRs 1–9 on our list have changes in temperature greater than 0.5 MK, however these events did not have other unusual properties with the exception of large changes in proton temperature.

[31] Figure 9 shows the evolution of CIR meridional tilt over the solar cycle. Plotted are: Day of Carrington rotation that the CIR was observed versus time (error bars represent the CIR duration) (Figure 9a), the meridional tilt, α of the planar events on our list (Figure 9b), and the solar dipole tilt (black), obtained from Wilcox Solar Observatory (WSO) data, and sunspot number (red) (Figure 9c).

[32] Figure 9a shows that CIRs only begin to recur regularly after 2004, during the decline to solar minimum 23. This provides further confidence in our CIR selection criteria since well-developed, recurring CIRs are more likely to form when the solar magnetic dipole is stable and tilted from the rotation axis, which is common during the decline to solar minimum [*Pizzo*, 1991]. Figure 9b shows that recurring planar CIRs show no relationship between their meridional tilts from one rotation to the next. The series of 6 CIRs (encircled) around September 2006 are all planar and have widely varying meridional tilts with no clear pattern. This is also shown for the other two sets of recurring CIRs. Another interesting result is that there is no dependence of CIR tilt on the phase of the solar cycle.

[33] Figure 10 shows the CIR meridional tilt versus the magnetic field polarity in the high speed stream for all the planar CIRs on our list that occurred after January 2004. We used CIRs from 2004 to 2008 because the Sun's magnetic field was in a relatively stable configuration during the minimum of solar cycle 23, with outward and inward polarity largely originating from the southern and northern hemispheres, respectively. We calculate the magnetic field polarity by subtracting the predicted Parker spiral angle [*Forsyth et al.*, 2001] from the average magnetic field azimuth; values near 0° indicate outward magnetic field polarity, while values near 180° have inward polarity. At high heliographic latitude (>10°), *Gosling et al.* [1993] have shown that CIRs are likely to be observed in quadrants I and IV. Near the ecliptic plane, however, Figure 10 shows that the meridional tilts of CIRs

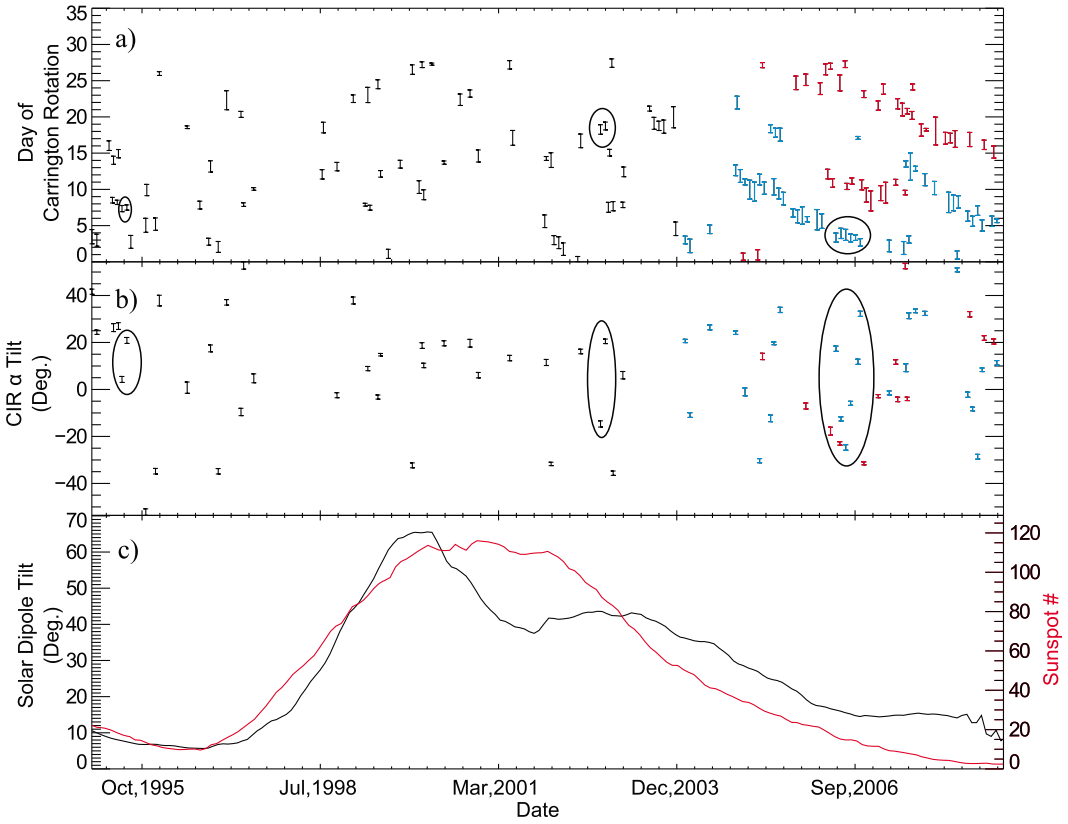

Figure 9. (a) Day of Carrington rotation of CIR occurrence over time, (b) CIR meridional tilt alpha over time, and (c) solar dipole tilt (black) and sunspot number (red) over time. In Figure 9a, events after Jan. 1, 2003 have been color coded based upon the magnetic field polarity of the high speed stream immediately following the CIR. Outward IMF events are colored red, while inward IMF events are colored blue. Black circles identify planar CIRs that were observed over at least two recurring Carrington rotations.

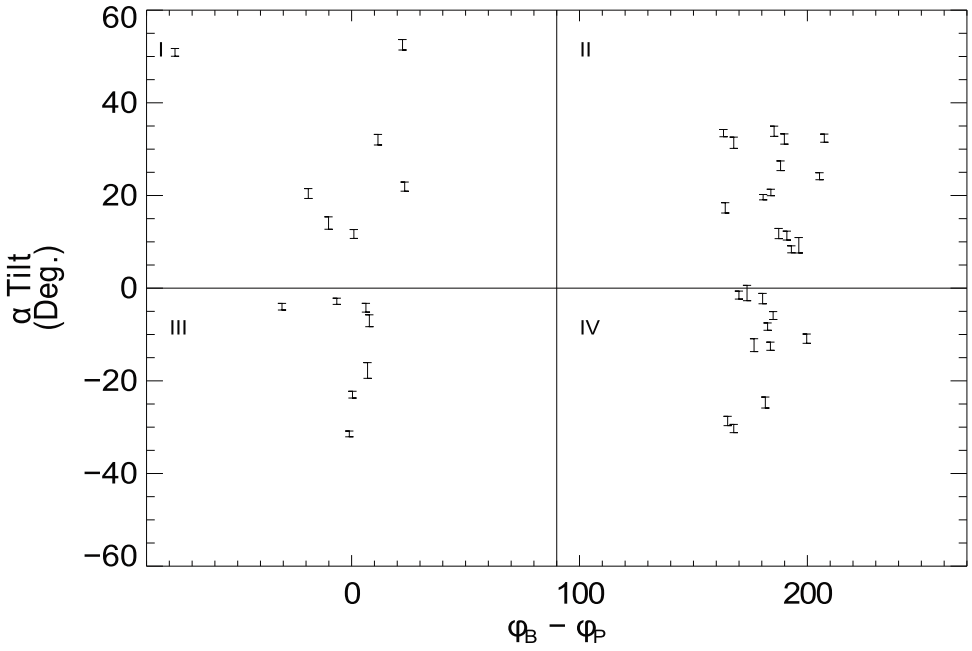

Figure 10. CIR meridional tilt versus the deviation of the average magnetic field azimuth from the predicted Parker spiral. Error bars show the uncertainty in the value of α.

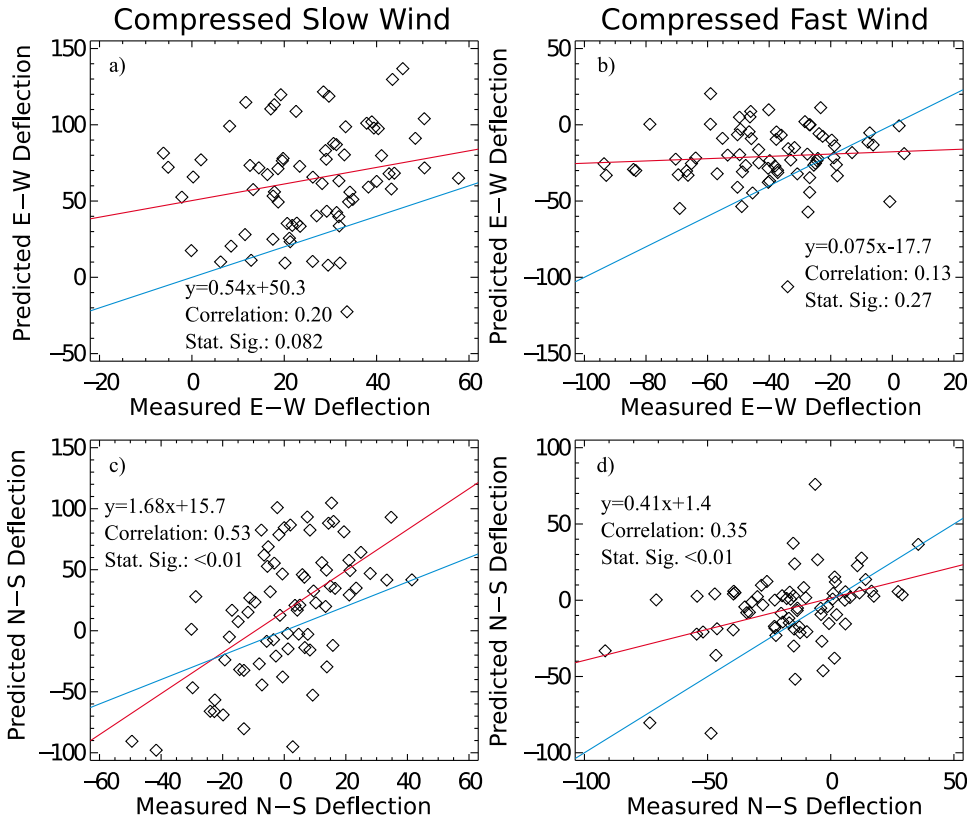

Figure 11. Lee's predicted versus observed solar wind deflections. Azimuthal deflections in (a) the compressed slow, (b) compressed fast solar wind and meridional deflection within (c) the compressed slow, and (d) compressed fast solar wind.

are not well ordered by the magnetic field polarity of the parent coronal hole.

3.4. Solar Wind Deflection and PMS Orientation in CIRs

[34] Figure 11 shows scatterplots of the predicted solar wind deflection by *Lee* [2000] versus the observed solar wind deflection. Figures 11a and 11b examine the azimuthal deflection of the compressed slow and fast wind respectively, while Figures 11c and 11d examine the meridional deflection in the same regions. The predicted solar wind deflection in both the azimuthal and meridional components are calculated in both the compressed slow and fast regions of the CIR using equations (20)–(23) in Lee's paper. We approximate the observed solar wind deflection by averaging the tangential and normal velocity components across the compressed slow (e.g., see Figure 2, region 2) and compressed fast (e.g., see Figure 2, region 3) regions of each CIR.

[35] The red line in each panel shows the linear fit between the predicted and the observed solar wind deflection components. There is a statistically significant relationship between the observed and predicted deflection out of the ecliptic (Figures 11c and 11d), indicating that the deflection is a function of solar wind speed and the shape of the CIR. However, the azimuthal deflection is not well correlated, and in the compressed fast wind there is no relationship at all (Figure 11b).

[36] Table 5 shows the results of a linear regression Student's t test, which compares the linear fits in Figure 11 to the ideal function of y = x (Figure 11, blue curve). From top to bottom, Table 5 contains azimuthal deflection in the compressed slow solar wind, azimuthal deflection in the compressed fast solar wind, meridional deflection in the compressed slow solar wind and meridional deflection in the compressed fast solar wind. Table 5 contains the results for both a and b in the function y = a + bx. The left four columns show results for the y-intercept, a, while the right four columns show the analysis for the slope, b. Within each four columns from left to right the table shows: the difference between the observed and expected coefficient, the standard error for the observed coefficient, the t-score for the observed deviation from the expected value and the probability that the observed coefficient supports the hypothetical value.

[37] Results shown in Table 5 indicate that it is unlikely that observed solar wind deflections behave according to the predictions of Lee's model. The only coefficient that strongly agrees with Lee's predictions is the y-intercept in the meridional deflection of the fast solar wind, which has a t-test probability of 0.66. However, the slope for the corresponding meridional deflection for the fast solar wind is unlikely to be related to the hypothetical slope of 1. In contrast, the observed slope of the azimuthal deflection in the slow solar wind could be consistent with a slope of 1, as it has a probability of 0.112, but in this case the observed

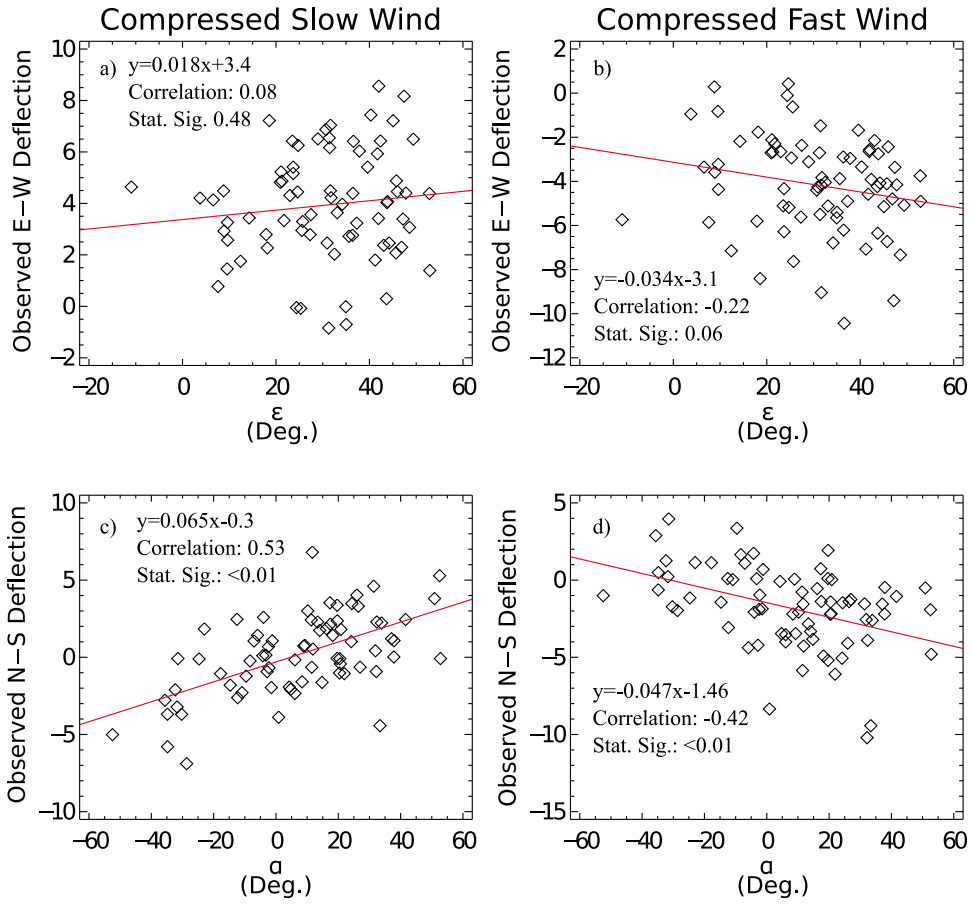

Figure 12. Solar wind deflection angles versus CIR tilt. The solar wind deflection angles and CIR tilts are compared in the same regions as Figure 11.

value of the y-intercept does not agree with Lee's predictions. Thus, it appears that the parameters of the four linear fits to the data do not agree with Lee's predictions.

[38] Figure 12 shows scatterplots of the average azimuthal flow angle in the compressed slow solar wind versus ε (Figure 12a), the average azimuthal flow angle in the compressed fast solar wind versus ε (Figure 12b), the average meridional flow angle in the compressed slow solar wind versus α (Figure 12c), and the average meridional flow angle in the compressed fast solar wind versus α (Figure 12d). Each panel also shows linear fits (red lines) to the data. Notice that the meridional flow angles are strongly related to α (Figures 12c and 12d), while the azimuthal flow angles and tilt (Figures 12a and 12b) exhibit a much weaker relationship. The linear relationships for the meridional deflection versus the meridional tilt are y = 0.065x – 0.3 in the compressed slow wind and y =−0.047x – 1.5 in the compressed fast wind.

4. Discussion

4.1. CIR Formation, Evolution, and Deflection of Solar Wind

[39] In this study we examined the bulk plasma, magnetic field properties, and structure of CIRs at 1 AU using ACE and Wind high resolution plasma and magnetic field data. We identified 153 CIRs using a semi-automated search algorithm. Within our list, we identified a subset of 74 (48.4%) planar CIRs using MVA. We compared the plasma and magnetic field properties of planar and non-planar events to study the formation of planar magnetic structures in CIRs. We then surveyed the three dimensional tilt, CIR width, and evolution over the solar cycle. We compared our results with predictions of Lee's theory of solar wind deflection in all 74 planar CIRs.

[40] Our analysis of 153 CIRs shows the following: (1) The dynamic, thermal, and magnetic pressures within CIRs are strongly correlated (Figure 5). (2) There is no statistical difference between planar and non-planar CIRs in the distributions and correlations between bulk plasma and magnetic field parameters (Figures 4 and 5). (3) The mean of observed CIR azimuthal tilt is 30.7 ± 13.5°, while the meridional tilt is 22.0 ± 12.9° and −17.2 ± 14.1° to the north and south respectively (Figure 6). (4) CIR widths observed at 1 AU have a lower limit of 0.25 ± 0.10 AU (Figure 7). (5) CIRs around solar maximum show the strongest compression (Figure 8). (6) The meridional tilt of CIRs changes significantly from one solar rotation to the next with no clear relationship between successive reoccurrences (Figure 9). (7) The meridional tilt of CIRs in the ecliptic is not ordered by the magnetic field polarity of the CIR's parent coronal hole (Figure 10). (8) The solar wind deflection is a

Table 5. Results of a T-Test Comparing the Linear Fits of Predicted Versus Observed Solar Wind Deflections Shown in Figure 10 to the Ideal Fit of $y = a_0 + b_0 * x$, Where a_0 and b_0 Equal 0 and 1, Respectively[a]

	$b-b_0$	SE_b	b T-Score	b Probability	$a-a_0$	SE_a	a T-Score	a Probability
Azimuthal deflection slow	−0.46	0.28	−1.61	0.112	50.3	8.2	6.1	4.5E-8
Azimuthal deflection fast	−0.92	0.11	−8.75	6.0E-13	−17.7	4.8	−3.7	4.3E-4
Meridional deflection slow	0.68	0.29	2.36	0.021	15.7	5.0	3.2	2.3E-3
Meridional deflection fast	−0.59	0.11	−5.59	3.8E-07	1.36	3.1	0.45	0.66

[a]From top to bottom, we show results for azimuthal deflection in the compressed slow solar wind, azimuthal deflection in the compressed fast solar wind, meridional deflection in the compressed slow solar wind and meridional deflection in the compressed fast solar wind.

function of CIR shape and speed, however the observed relationship is not in quantitative agreement with that predicted by Lee's model (Figure 11). (9) There is a strong correlation between the CIR meridional tilt and the solar wind meridional deflection angle, but not between the azimuthal tilt and solar wind deflection angles (Figures 11 and 12).

[41] We observed the change in solar wind speed across the forward and reverse boundaries to be 360 ± 76 km s^{-1}, while *Jian et al.* [2006] observed a value of 230 ± 93 km s^{-1}. In addition to change in speed across the event, Jian et al. also studied the peak in total pressure. They found a mean of 176 ± 108 pPa, which is similar to the value that we observed of 214 ± 109 pPa. We observed larger changes in speed and higher levels of compression in our CIRs, probably because we only included stronger events with a minimum speed below 450 km s^{-1} and a maximum above 550 km s^{-1}, a peak in proton density above 20 cm^{-3}, and a peak in total pressure above 100 pPa.

[42] Figure 5 showed that the strongest relationship between CIR properties existed between the different types of pressure. This result is interesting, but not surprising because CIRs are pressure waves [*Lee*, 2000; *Pizzo*, 1991]. Solar wind energy is predominantly in the dynamic pressure, but compression within the CIR transfers some of that energy into thermal and magnetic pressure. The relationships between magnetic field strength versus solar wind speed and magnetic field strength versus proton density probably occurs because they are related to the dynamic, magnetic, and thermal pressures.

[43] Table 4 shows that there is no statistical difference between planar and non-planar CIRs. This result is surprising, because *Neugebauer et al.* [1993] suggested that compression or draping of field lines along the leading edge of high speed streams may be a possible cause for heliospheric PMSs. Additionally, it has been proposed by *Clack et al.* [2000] that stronger compression may enhance the planarity of the IMF. Approximately 20% of our CIRs had forward or reverse shocks (section 2.2); beyond 3 AU most CIRs have developed shocks [*Gosling and Pizzo*, 1999]. Therefore, more magnetically planar CIRs may be seen beyond

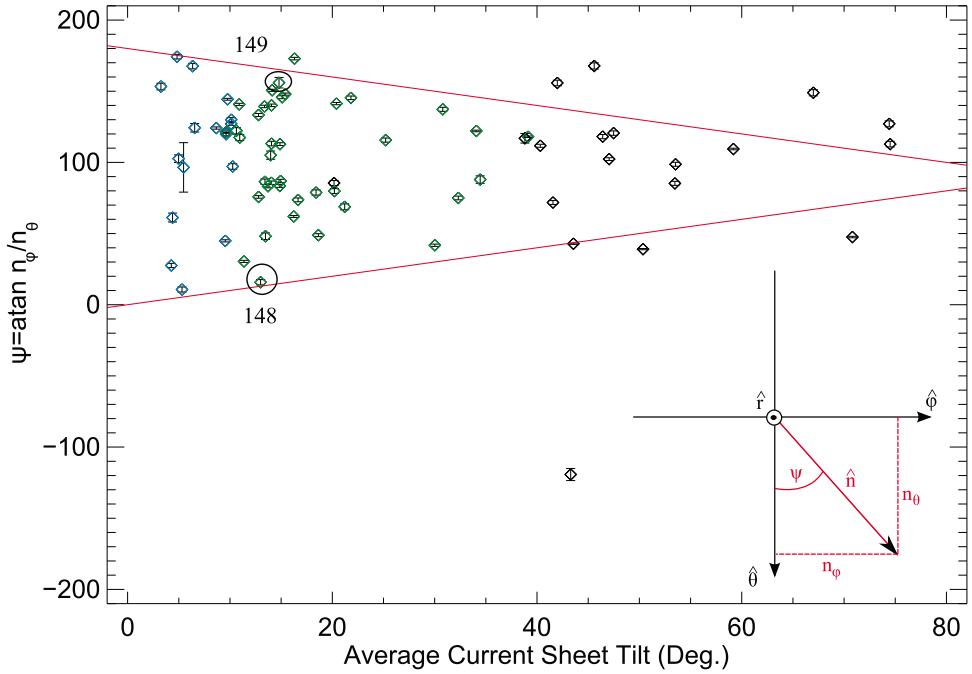

Figure 13. A comparison of CIR orientation to the average heliospheric current sheet tilt. CIRs from before Jan. 1, 1998 are blue, CIRs after Jan. 1, 2004 are green and those in between are black. Uncertainty in ψ is shown with black error bars for each event. The solid red line represents the predicted behavior for CIRs produced by large circular coronal holes [*Lee*, 2000]. The two circled events are numbers 148 and 149 on our list. We have also included a coordinate system relating ψ to **n** in the φ-θ (T-N) plane.

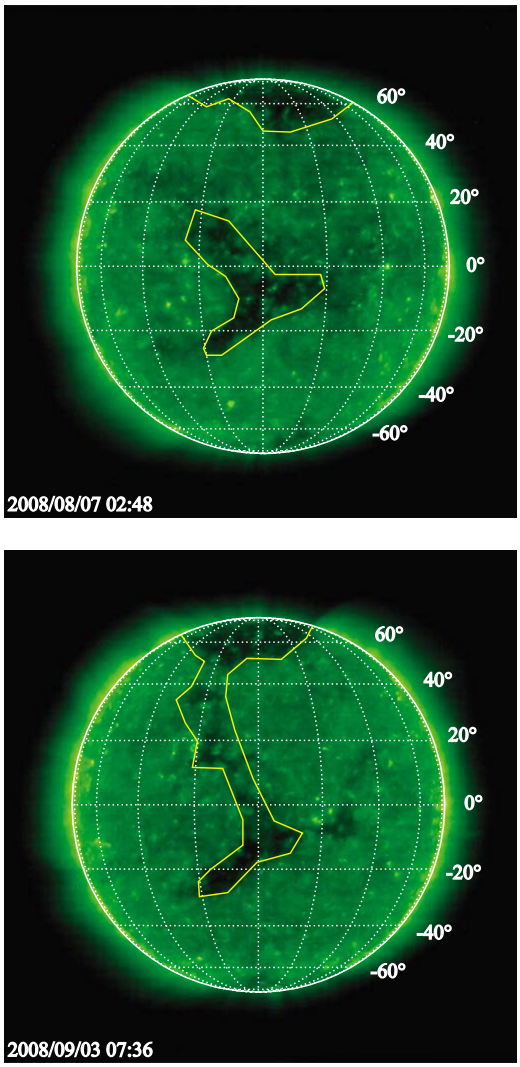

Figure 14. SOHO EIT 195 Å images of the coronal holes that produced CIRs 148 and 149 on our list. The associated coronal hole has been outlined in yellow and white grid lines show the latitude and longitude in 20° increments.

Earth orbit; for example at Ulysses. We suggest that a statistically significant difference in behavior might be observed with a larger sample of CIRs.

[44] The average tilt out of the ecliptic is near 20° in both the north and south directions, while the azimuthal tilt is close to one standard deviation from the normal of the average predicted Parker spiral at 1 AU [*Forsyth et al.*, 2001]. This qualitatively agrees with theory [*Lee*, 2000; *Pizzo*, 1991], which states that the CIR pressure wave forms along the stream interface between the fast and slow solar wind streams. However, a comparison of the CIR azimuthal tilt to the predicted Parker spiral using solar wind speed as described by *Forsyth et al.* [2001] for the planar events (not shown) showed no relationship. The asymmetric occurrence of CIRs with northern tilt is interesting; however it is unlikely that we have encountered more CIRs generated by coronal holes from the southern hemisphere as might be expected from CIRs surveyed at higher latitudes and larger radial distances [*Gosling et al.*, 1993], because Figure 10 shows that CIR tilt observed near the ecliptic does not depend on the polarity of the coronal hole.

[45] We also estimate the CIR thickness at 1 AU to be 0.25 ± 0.10 AU with a radial width of 0.33 ± 0.14 AU. This is similar to the radial width value of 0.41 AU that *Jian et al.* [2006] report. The radial width is dependent upon both the minimum width and the tilt of a CIR. Thus it appears that radial width provides an estimate, while the minimum width Δx provides a lower limit for the scale size of the CIR.

[46] We have also studied the annual variation of CIR properties. Figure 8 shows that the strongest compression within CIRs during the last solar cycle occurred during solar maximum. This is in good agreement with results from *Jian et al.* [2006]. To the best of our knowledge, we know of no other large statistical surveys for CIRs at 1 AU that studied solar cycle variations before 1995. Thus, due to the extended length of solar cycle 23, it is difficult to determine if the reduced compression during solar minimum is typical or might be a unique feature related to the reduced open magnetic flux and solar wind dynamic pressure of this solar cycle [*McComas et al.*, 2008; *Smith and Balogh*, 2008].

[47] Figure 9 examined the behavior of CIR tilt over multiple Carrington rotations as well as over the solar cycle. Figure 9b shows that the tilt out of the ecliptic is not related to the meridional tilt of the previous appearance of the CIR. *Pizzo et al.* [1995] suggested that the local structure of the coronal hole is important in the shape of the CIR observed in the heliosphere. They also suggest that this local structure might change rapidly at the ecliptic because of complex rotational effects. More recently, the idea of a complex coronal hole structure has been predicted [*Antiochos et al.*, 2010] and possibly observed [*Crooker et al.*, 2010]. It would be useful to compare the tilt of the same CIR at multiple spacecraft, in particular ACE, Wind, STEREO A, and B. As STEREO A and B become farther apart, there is an opportunity to study the three dimensional evolution of CIRs on timescales shorter than one Carrington rotation. Additionally in 2007 all four of these spacecraft were relatively close to one another, permitting a fully three dimensional study of CIR magnetic structure [*Dunlop and Woodward*, 1998]. However, such a multi-spacecraft study of CIRs is beyond the scope of the present work and will be the subject of a future study. We also find no clear relationship of CIR tilt to the solar cycle in Figure 9, as one might expect if the CIRs meridional tilt only depended on large, circular polar coronal holes tilted by some angle from the solar rotation axis [*Lee*, 2000; *Pizzo*, 1991].

[48] Based on the 1992–1994 Ulysses observations of CIRs at higher heliographic latitudes during the declining phase of the previous solar cycle [*Gosling et al.*, 1993] and theoretical studies of *Lee* [2000], one might also expect the CIR meridional tilt to be ordered according to the polarity of the parent coronal hole. However, this is in contrast to the results shown in Figure 10, which could be due to the fact that our observations are at 1 AU near the ecliptic plane where the CIRs are not fully formed and are likely to originate from equatorward extensions of polar coronal holes as well as from smaller, irregular, equatorial coronal holes (e.g., see Figure 14, top).

[49] In Figure 11 we compared Lee's prediction of solar wind deflection to observations of solar wind deflection

during solar cycles 22 and 23. *Clack et al.* [2000] qualitatively showed that CIRs with southern tilt deflect the solar wind east and south ahead and west and north behind, while producing deflections east and north ahead and west and south behind CIRs with northern tilt [*Gosling et al.*, 1993]. We have quantitatively compared Lee's theory with observations for 74 events. Our results indicate Lee's current theory does not quantitatively describe the observed relationship at 1 AU. One possible reason might be because Lee's model and MVA both assume a perfectly planar structure; whereas higher order curvature within the CIR could cause local deviations from the predicted solar wind deflections. Lee's model also assumes that the boundaries of the CIRs have steepened into shocks, however our list contained only 19 CIRs (∼12.4%) with forward shocks and 13 CIRs (∼8.5%) with reverse shocks. We also note that none of our CIRs had both forward and reverse shocks at the same time.

[50] Figure 12 quantitatively relates solar wind deflection angles to CIR tilt. Azimuthal deflection is not well correlated with the azimuthal tilt of the CIR. It is unclear why this is the case, while the meridional deflection angles and tilts show a strong relationship for the 74 CIRs. We suggest that comparing the relationships of CIRs at Ulysses to those observed at 1 AU may yield a better understanding of how the presence of shocks affects the deflection of solar wind, because forward and reverse shocks are much more common at those distances.

4.2. CIRs and Coronal Hole Shape

[51] In order to relate the CIR's shape at 1 AU back to the solar surface, we have adapted *Lee*'s [2000] prediction and compared it with our observations. Lee relates the shape of the CIR back to the Sun for two separate scenarios; (1) a large circular coronal hole tilted by the solar dipole tilt angle from the solar rotation axis, and (2) an arbitrarily shaped coronal hole that has a smooth boundary with constant slope across its leading edge. By approximating the WSO average HCS tilt for the solar dipole tilt, we can quantitatively compare our observations with Lee's first scenario for all planar CIRs. We also perform a case study by comparing two events to the shape of their potential parent coronal hole to investigate whether the second scenario could account for our observations.

[52] Figure 13 relates the arctan n_φ/n_θ (which we call ψ) to the average HCS tilt, t. We note that *Pizzo* [1991] calls ψ the inclination angle, ι, and they describe it as the orientation of the CIR front with respect to the θ-φ plane. The two normal vector components, n_φ and n_θ, are equivalent to n_T and $-n_N$ respectively in the RTN coordinate system. The inserted diagram describes the orientation of ψ when viewed from the Earth towards the Sun. Uncertainty in ψ has been propagated from the uncertainty in the normal vector components, which we determined using a technique developed by *Kawano and Higuchi* [1995]. The solid red lines are $\psi = t$ for northern coronal holes and $\psi = 180 - t$ for southern coronal holes, when observed from the heliographic equator. The two equations for ψ are derived from equation (24) of *Lee* [2000], which predicts the tilt of the CIR produced by a circular polar coronal hole tilted by the solar dipole tilt from the solar rotation axis. Lee's model applies to any solar dipole tilt from 0 to 180 degrees, however the average Wilcox Solar Observatory current sheet data only provides absolute values of the tilt angle between 0 and 90. Therefore, we used the second equation above to relate t to ψ for CIRs from southern coronal holes. Events before Jan. 1, 1998 are colored blue, those after Jan. 1, 2004 are colored green and all events in between are shown as black. These colors identify events that occurred in solar minimum 22, solar minimum 23, and solar maximum 22, respectively. Figure 13 shows several results: (1) the average current sheet tilt is well ordered by the solar cycle, (2) very few CIRs behave according to Lee's predictions for large circular polar coronal holes, and (3) with one exception, all of the solar minimum CIRs fall within the boundaries of Lee's predicted model.

[53] The first result is easily explained by considering the heliospheric current sheet data over the solar cycle (Figure 9c). In particular, note that the HCS tilt during solar minimum 23 was larger (∼20°) than that during solar minimum 22 (∼5°) and solar maximum was more tilted than either minimum (∼65°). The second result suggests that assuming coronal holes to be circular is not a realistic approximation, even during solar minimum conditions. Finally, it is interesting that Lee's prediction seems to bound the angle ψ so well during solar minimum. The CIRs when ψ is near 90° have the largest azimuthal component in the normal vector relative to the meridional component. We have used the average HCS tilt as a proxy for solar dipole tilt, however, this value does not account for warping of the current sheet or for small-scale structure within the coronal holes. Deviation away from a perfectly circular shape would result in some boundary normal vectors that are more azimuthal and some that are largely meridional. At the Sun, the boundary normal between fast and slow wind must have an azimuthal component or a CIR will not form out in the heliosphere [*Lee*, 2000]. We speculate that interfaces with particularly large meridional components to their normal vector do not strengthen into full CIRs. During solar maximum conditions the average HCS tilt is not a realistic approximation, which may be why so many solar maximum CIRs fall outside the boundaries.

[54] We have identified CIRs # 148 and 149 on our list to perform a case study because they occur about one Carrington rotation apart. Their ψ angles are remarkably different; however they have a similar value of n_φ and nearly opposite values of n_θ. In Figure 14 we identify their parent coronal hole: Figure 14 (top) shows the hole when it could have produced CIR 148, while Figure 14 (bottom) shows the same coronal hole when it may have produced CIR 149. Latitude and longitude are shown with the equator centered on the observation latitude of the SOHO spacecraft [*Domingo et al.*, 1995] and the outline of the coronal hole's basic shape is included in each image.

[55] At the equator, the leading edge of the coronal hole suggests that n_θ should be negative (a positive meridional tilt α), however only one of the CIRs at 1 AU actually reflects this. It is possible that fine structure along the boundary of the coronal hole plays a key role in defining the three dimensional shape of the CIR that it produces, and also that the coronal hole boundary is more complex than has been currently observed [*Antiochos et al.*, 2010; *Crooker et al.*, 2010]. This leads us to suggest that approximating the leading edge of a coronal hole as smooth

is also unrealistic. Thus our results indicate that to fully characterize the three-dimensional shape of a CIR in the heliosphere, the shape of the parent coronal hole must be better understood. It would be interesting to compare our observations with more complex MHD models of CIRs that do not make assumptions on coronal hole shape [e.g., *Riley*, 2007], but such a study is beyond the scope of this paper. Another possibility is that the CIR's shape evolves in interplanetary space. Several theory papers [*Gosling and Pizzo*, 1999; *Lee*, 2000; *Pizzo*, 1991] make predictions on how CIRs evolve in the heliosphere, however these require multiple spacecraft that are radially aligned. So more observational evidence is needed to investigate how CIR tilts evolve in the heliosphere.

Appendix A: Detailed Explanation of Our CIR Identification Algorithm

[56] Our algorithm for identifying CIRs uses the following steps:

1) Identification of slow-to-fast solar wind speed intervals: We identify the time interval by searching for periods when at least 10 data points simultaneously satisfy the three criteria listed below.

a) Increasing running average of solar wind speed (Figure 2a).

b) Increasing running average of solar wind temperature (Figure 2c).

c) Enhanced magnetic field compared to the background, e.g., in Figure 2e the magnetic field is enhanced ($\sim$10–20 nT) in regions 2 and 3 compared to the background IMF ($\sim$2–5 nT) located in regions 1 and 4.

Our algorithm includes additional data points as part of this candidate interval if they also satisfy the above three conditions and if they occur within a two-hour window of the last included data point. The interval is complete when no other data points meet these conditions within the two hour window. Using these broad selection criteria, we identified 7309 slow-to-fast solar wind speed intervals.

2). Elimination of weak intervals: For each slow-to-fast solar wind speed interval identified above, we compute the average time of all the data points. We only include intervals from the above list if they meet the conditions listed below within a two day window and if the new interval occurs at least 1.5 days after the previous interval. This criterion reduced the number of intervals down to 373.

a) The solar wind speed is less than 450 km s^{-1} in the first half of the two day window and increases above 550 km s^{-1} during the interval (Figure 2a).

b) The proton density increases above 20 cm^{-3} (Figure 2b).

c) The total pressure increases above 100 pPa (Figure 2d).

3) Selection of the forward boundary. We could not identify a forward boundary for 23 intervals, which reduced our list of intervals down to 350.

a) For the forward and reverse boundary we initially search for forward and reverse shocks, but these only exist in about 24% of CIRs at 1 AU [*Jian et al.*, 2006]. Shocks are identified by the shock lists for ACE (http://www.ssg.sr.unh.edu/mag/ace/ACElists/obs_list.html) or Wind (http://www-istp.gsfc.nasa.gov/wind/current_listIPS.htm).

b) If a forward shock is not present, the algorithm identifies the time when an abrupt and simultaneous increase is observed in 1) total pressure (Figure 2d), 2) magnetic field strength (Figure 2e), 3) proton speed (Figure 2a), 4) proton density (Figure 2b), and 5) proton temperature (Figure 2c). We define abrupt increases as the top 5% of slopes for the running averages of all 5 parameters between 1 day before and 3 days after an interval.

c) If no instances of abrupt and simultaneous increases are found, then the algorithm systematically removes parameters in the reverse order they appear in b) and repeats the search in the remaining parameters. This process continues until the algorithm identifies simultaneous increases in the remaining parameters or only the total pressure remains.

d) If multiple times meet the requirements in b) or c) then the algorithm selects the time with the largest increase in total pressure. We note that if the total pressure is the only remaining parameter, then this step occurs automatically because a single time cannot be identified otherwise.

4) Selection of reverse boundary. We could not identify a reverse boundary for 3 intervals, which reduced the total number of intervals to 347.

a) The identification process is similar to forward boundary selection, however we search for a simultaneous decrease in total pressure (Figure 2d), magnetic field strength (Figure 2e), proton density (Figure 2b), accompanied by an abrupt increase in solar wind speed (Figure 2a).

5) Selection of stream interface. We could not identify a stream interface in 3 intervals, which reduced the number of slow-to-fast solar wind speed intervals to 344.

a) The algorithm searches for a stream interface between the times of the forward and reverse boundaries. The stream interface is identified as an abrupt decrease in proton density (Figure 2b) accompanied by an abrupt increase in solar wind speed (Figure 2a) and temperature (Figure 2c).

b) The solar wind azimuthal deflection is close to 0 at the stream interface [*Gosling et al.*, 1978]. The algorithm requires that at the stream interface, the absolute value of azimuthal deflection, $|v_T|$, must be less than 5% of its maximum value between the forward and reverse boundary.

6) Removal of slow-to-fast solar wind speed intervals that are ICMEs, possible ICMEs, and those that occur in close proximity to a known ICME. Specifically, we removed 84 intervals that were identified as ICMEs by *Cane and Richardson* [2003] (updated list) and 13 intervals that exhibited ICME-like signatures (see Table 1). We also removed 41 intervals that occurred either in close proximity to an ICME on the Cane and Richardson list or in association with a transient forward shock. This reduced our list of slow-to-fast solar wind speed transition intervals to 206.

a) Possible ICMEs are identified using an updated version (see at http://www.ssg.sr.unh.edu/mag/ace/ACElists/ICMEtable.html) of the ICME list of *Cane and Richardson* [2003] or if they exhibit at least two of the following three well-known ICME signatures. We also verified the ICME-like intervals via a visually inspection.

1. The proton temperature is less than half of the expected temperature [*Neugebauer et al.*, 2003; *Richardson* and Cane, 1995].

2. The He/p ratio is above 8% [*Hirshberg et al.*, 1972].

3. The plasma β is less than 0.1 [*Klein and Burlaga*, 1982].

b) We also visually inspected and removed all intervals where transient forward shocks were identified in ACE and Wind shock lists (http://www.ssg.sr.unh.edu/mag/ace/ACElists/obs_list.html and http://www-istp.gsfc.nasa.gov/wind/current_listIPS.htm). Note that these intervals did not exhibit *in-situ* signatures of ICMEs as listed in 6a; but the presence of a transient forward shock implies that an ICME driver gas is responsible [e.g., *Gosling*, 1993].

7) Removal of intervals with weak secondary compressions or data gaps. Excluding these intervals reduced our list to 153 CIRs.

a) We removed CIRs with weak, secondary compressions if they occurred within two days of another CIR on our list.

b) We removed intervals when data gaps were present either inside of the boundaries or within 2 days surrounding an interval.

8) We define the end of the high speed stream as the time when Alfvén waves are no longer observed after the reverse boundary [*Tsurutani et al.*, 1995].

[57] **Acknowledgments.** This work is supported by the Southwest Research Institute. We thank the instrument teams and PI's for SWEPAM, SWE (K.W. Ogilvie), MAG (C.W. Smith) and MFI (R.P. Lepping) for their work. We are grateful to Joey Mukherjee and Jillian Redfern for their help in software development. Additionally we thank Richard Menchaca for his help in modifying Figure 1 in our paper. We also wish to thank the creators of the ICME list (H.V. Cane and I.G. Richardson) and two shock lists (C.W. Smith and J.C. Kasper) that we have used in our analysis. We also thank those at Wilcox Solar Observatory who helped in the development of the heliospheric current sheet tilt data. Work has been supported by the NASA grants NNX08AK87G, and NNX07AG85G and the NSF grant ATM-0962666.

[58] Philippa Browning thanks the reviewers for their assistance in evaluating this paper.

References

Acuña, M. H., K. W. Ogilvie, D. N. Baker, S. A. Curtis, D. H. Fairfield, and W. H. Mish (1995), The Global Geospace Science Program and its investigations, *Space Sci. Rev.*, *71*, 5–21.

Antiochos, S. K., Z. Mikic, R. Lionello, V. Titov, and J. Linker (2010), A model for the sources of the slow solar wind, *Bull. Am. Astron. Soc.*, *41*, 892. [Available at http://adsabs.harvard.edu/abs/2010AAS…21640521A.]

Belcher, J. W., and L. Davis (1971), Large-amplitude Alfvén waves in the interplanetary medium, 2, *J. Geophys. Res.*, *76*, 3534–3563.

Borovsky, J. E., and M. H. Denton (2010), Solar wind turbulence and shear: A superposed-epoch analysis of corotating interaction regions at 1 AU, *J. Geophys. Res.*, *115*, A10101, doi:10.1029/2009JA014966.

Borrini, G., J. M. Wilcox, J. T. Gosling, S. J. Bame, and W. C. Feldman (1981), Solar wind helium and hydrogen structure near the heliospheric current sheet: A signal of coronal streamers at 1 AU, *J. Geophys. Res.*, *86*, 4565–4573.

Cane, H. V., and I. G. Richardson (2003), Interplanetary coronal mass ejections in the near-Earth solar wind during 1996–2002, *J. Geophys. Res.*, *108*(A4), 1156, doi:10.1029/2002JA009817.

Clack, D., R. J. Forsyth, and M. W. Dunlop (2000), Ulysses observations of the magnetic field structure within CIRs, *Geophys. Res. Lett.*, *27*, 625.

Crooker, N. U., E. M. Appleton, N. A. Schwadron, and M. J. Owens (2010), Suprathermal electron flux peaks at stream interfaces: Signature of solar wind dynamics or tracer for open magnetic flux transport on the Sun?, *J. Geophys. Res.*, *115*, A11101, doi:10.1029/2010JA015496.

Domingo, V., B. Fleck, and A. I. Poland (1995), The SOHO Mission: An Overview, *Sol. Phys.*, *162*, 1–37.

Dunlop, M. W., and T. I. Woodward (1998), Multi-spacecraft discontinuity analysis: Orientation and motion, in *Analysis Methods for Multi-Spacecraft Data*, edited by G. Paschmann and P. Daly, *ISSI Sci. Rep. Ser., SR-001*, 271–306.

Forsyth, R. J., A. Balogh, and E. J. Smith (2001), Latitudinal variation of the underlying heliospheric magnetic field direction: Comparison of the Ulysses first and second orbits. *Space Sci. Rev.*, *97*, 161–164.

Gosling, J. T. (1993), The solar flare myth, *J. Geophys. Res.*, *98*, 18,937–18,950.

Gosling, J. T., and V. J. Pizzo (1999), Formation and evolution of corotating interaction regions and their three dimensional structure, *Space Sci. Rev.*, *89*, 21–52.

Gosling, J. T., V. Pizzo, and S. J. Bame (1973), Anomalously low proton temperatures in the solar wind following interplanetary shock waves—Evidence for magnetic bottles?, *J. Geophys. Res.*, *78*, 2001–2009.

Gosling, J. T., J. R. Asbridge, S. J. Bame, and W. C. Feldman (1978), Solar wind stream interfaces, *J. Geophys. Res.*, *83*, 1401–1412.

Gosling, J. T., D. N. Baker, S. J. Bame, W. C. Feldman, R. D. Zwickl, and E. J. Smith (1987), Bidirectional solar wind electron heat flux events, *J. Geophys. Res.*, *92*(A8), 8519–8535, doi:198710.1029/JA092iA08p08519.

Gosling, J. T., S. J. Bame, D. J. McComas, J. L. Phillips, V. J. Pizzo, B. E. Goldstein, and M. Neugebauer (1993), Latitudinal variation of solar wind corotating stream interaction regions: ULYSSES, *Geophys. Res. Lett.*, *20*, 2789–2792.

Hirshberg, J., S. J. Bame, and D. E. Robbins (1972), Solar flares and solar wind helium enrichments: July 1965 July 1967, *Sol. Phys.*, *23*, 467–486.

Intriligator, D. S., J. R. Jokipii, T. S. Horbury, J. M. Intriligator, R. J. Forsyth, H. Kunow, G. Wibberenz, and J. T. Gosling (2001), Processes associated with particle transport in corotating interaction regions and near stream interfaces, *J. Geophys. Res.*, *106*, 10,625–10,634.

Jian, L., C. T. Russell, J. T. Gosling, and J. G. Luhmann (2005), Measurements of heating at stream-stream interactions, in *Proceedings of the Solar Wind 11/SOHO 16 Connecting Sun and Heliosphere Conference, 12–17 June 2005, Whistler, Canada*, edited by B. Fleck, T. H. Zurbuchen, and H. Lacoste, *ESA Spec. Publ.*, *SP-592*, 491. [Available at http://adsabs.harvard.edu/abs/2005ESASP.592E..89J.]

Jian, L., C. T. Russell, J. G. Luhmann, and R. M. Skoug (2006), Properties of stream interactions at one AU during 1995–2004, *Sol. Phys.*, *239*, 337–392.

Jones, G. H., and A. Balogh (2000), Context and heliographic dependence of heliospheric planar magnetic structures, *J. Geophys. Res.*, *105*(A6), 12,713–12,724.

Jones, G. H., A. Balogh, and T. S. Horbury (1999), Observations of heliospheric planar and offset-planar magnetic structures, *Geophys. Res. Lett.*, *26*, 13–16.

Kawano, H., and T. Higuchi (1995), The bootstrap method in space physics: Error estimation for the minimum variance analysis, *Geophys. Res. Lett.*, *22*(3), 307–310, doi:199510.1029/94GL02969.

Khrabrov, A. V., and B. U. Ö. Sonnerup (1998), Error estimates for minimum variance analysis, *J. Geophys. Res.*, *103*, 6641–6652.

Klein, L. W., and L. F. Burlaga (1982), Interplanetary magnetic clouds at 1 AU, *J. Geophys. Res.*, *87*, 613–624.

Lee, M. A. (2000), An analytical theory of the morphology, flows, and shock compressions at corotating interaction regions in the solar wind, *J. Geophys. Res.*, *105*, 10,491–10,500.

Lepping, R. P., et al. (1995), The wind magnetic field investigation, *Space Sci. Rev.*, *71*, 207–229.

McComas, D. J., S. J. Bame, P. Barker, W. C. Feldman, J. L. Phillips, P. Riley, and J. W. Griffee (1998), Solar Wind Electron Proton Alpha Monitor (SWEPAM) for the Advanced Composition Explorer, *Space Sci. Rev.*, *86*, 563–612.

McComas, D. J., R. W. Ebert, H. A. Elliott, B. E. Goldstein, J. T. Gosling, N. A. Schwadron, and R. M. Skoug (2008), Weaker solar wind from the polar coronal holes and the whole Sun, *Geophys. Res. Lett.*, *35*, L18103, doi:10.1029/2008GL034896.

Nakagawa, T., A. Nishida, and T. Saito (1989), Planar magnetic structures in the solar wind, *J. Geophys. Res.*, *94*, 11,761–11,775.

Neugebauer, M., and C. W. Snyder (1966), Mariner 2 observations of the solar wind: 1. Average properties, *J. Geophys. Res.*, *71*, 4469.

Neugebauer, M., and C. W. Snyder (1967), Mariner 2 observations of the solar wind: 2. Relation of plasma properties to the magnetic field, *J. Geophys. Res.*, *72*, 1823.

Neugebauer, M., D. R. Clay, and J. T. Gosling (1993), The origins of planar magnetic structures in the solar wind, *J. Geophys. Res.*, *98*, 9383–9389.

Neugebauer, M., J. T. Steinberg, R. L. Tokar, B. L. Barraclough, E. E. Dors, R. C. Wiens, D. E. Gingerich, D. Luckey, and D. B. Whiteaker (2003), Genesis on-board determination of the solar wind flow regime, *Space Sci. Rev.*, *105*(3), 661–679, doi:10.1023/A:1024478129261.

Ogilvie, K. W., et al. (1995), SWE, a comprehensive plasma instrument for the Wind spacecraft, *Space Sci. Rev.*, *71*, 55–77.

Paschmann, G., and P. W. Daly (1998), *Analysis Methods for Multi-Spacecraft Data*, edited by G. Paschmann and P. Daly, *ISSI Sci. Rep. Ser., SR-001*. [Available at http://adsabs.harvard.edu/abs/1998ISSIR…1.....P.]

Pizzo, V. J. (1991), The evolution of corotating stream fronts near the ecliptic plane in the inner solar system: 2. Three-dimensional tilted-dipole fronts, *J. Geophys. Res.*, *96*, 5405–5420.

Pizzo, V. J., D. S. Intriligator, and G. L. Siscoe (1995), Radial alignment simulation of solar wind streams observed by Pioneers 10 and 11 in 1974, *J. Geophys. Res.*, *100*, 12,251.

Richardson, I. G., and H. V. Cane (1995), Regions of abnormally low proton temperature in the solar wind (1965–1991) and their association with ejecta, *J. Geophys. Res.*, *100*, 23,397–23,412.

Ridley, A. J. (2000), Estimations of the uncertainty in timing the relationship between magnetospheric and solar wind processes, *J. Atmos. Sol. Terr. Phys.*, *62*, 757–771.

Riley, P. (2007), Modeling corotating interaction regions: From the Sun to 1 AU, *J. Atmos. Sol. Terr. Phys.*, *69*, 32–42.

Riley, P., J. T. Gosling, L. A. Weiss, and V. J. Pizzo (1996), The tilts of corotating interaction regions at midheliographic latitudes, *J. Geophys. Res.*, *101*, 24,349–24,358.

Rouillard, A. P., et al. (2009), A multispacecraft analysis of a small-scale transient entrained by solar wind streams, *Sol. Phys.*, *256*(1-2), 307–326, doi:10.1007/s11207-009-9329-6.

Russell, C. T., A. A. Shinde, and L. Jian (2005), A new parameter to define interplanetary coronal mass ejections, *Adv. Space Res.*, *35*(12), 2178–2184, doi:10.1016/j.asr.2005.04.024.

Skoug, R. M., J. T. Steinberg, K. A. Goodrich, and B. R. Anderson (2010), Solar wind suprathermal electron Strahl widths across high speed stream structures, Abstract SH34A-04 presented at 2010 Fall Meeting, AGU, San Francisco, Calif.

Smith, C. W., J. L'Heureux, N. F. Ness, M. H. Acuña, L. F. Burlaga, and J. Scheifele (1998), The ACE Magnetic Fields Experiment, *Space Sci. Rev.*, *86*, 613–632.

Smith, E. J., and A. Balogh (2008), Decrease in heliospheric magnetic flux in this solar minimum: Recent Ulysses magnetic field observations, *Geophys. Res. Lett.*, *35*, L22103, doi:10.1029/2008GL035345.

Sonnerup, B. U. O., and L. J. Cahill (1967), Magnetopause structure and attitude from Explorer 12 observations, *J. Geophys. Res.*, *72*, 171.

Stone, E. C., A. M. Frandsen, R. A. Mewaldt, E. R. Christian, D. Margolies, J. F. Ormes, and F. Snow (1998), The Advanced Composition Explorer, *Space Sci. Rev.*, *86*, 1–22.

Tsurutani, B. T., C. M. Ho, J. K. Arballo, B. E. Goldstein, and A. Balogh (1995), Large amplitude IMF fluctuations in corotating interaction regions: Ulysses at midlatitudes, *Geophys. Res. Lett.*, *22*, 3397–3400.

Wimmer-Schweingruber, R. F., R. von Steiger, and R. Paerli (1997), Solar wind stream interfaces in corotating interaction regions: SWICS/Ulysses results, *J. Geophys. Res.*, *102*, 17,407–17,418.

Zurbuchen, T. H., and I. G. Richardson (2006), In-situ solar wind and magnetic field signatures of interplanetary coronal mass ejections. *Space Sci. Rev.*, *123*, 31–43.

T. W. Broiles, M. I. Desai, and D. J. McComas, Space Science and Engineering Division, Southwest Research Institute, 6220 Culebra Rd., San Antonio, TX 78238-5166, USA. (tbroiles@swri.edu)